Mechanisms of gene regulation by SRCAP and H2A.Z

Armelle Tollenaere[1*], Enes Ugur[2,3,5], Susanna Dalla-Longa[4,5], Cédric Deluz[1], Devin Assenheimer[4], J Christof M Gebhardt[4], Heinrich Leonhardt[3], David M Suter[1*]

[1]Ecole Polytechnique Fédérale de Lausanne, School of Life Sciences, Institute of Bioengineering, Lausanne, Switzerland
[2]Department of Proteomics and Signal Transduction, Max-Planck Institute of Biochemistry, Martinsried 82152, Germany.
[3]Faculty of Biology and Center for Molecular Biosystems (BioSysM), Human Biology and BioImaging, Ludwig-Maximilians-Universität München, Munich 81377, Germany.
[4]Institute of Experimental Physics and IQST, Ulm University, Albert-Einstein-Allee 11, 89081, Germany
[5]These authors contributed equally to this work

*Corresponding authors: armelle.tollenaere@epfl.ch (AT) and david.suter@epfl.ch (DS)

Abstract

Discriminating regulatory functions of chromatin composition from those of chromatin-modifying complexes is a central problem in gene regulation. This question remains unexplored in the context of histone variants and their dedicated chromatin remodelers. Here we dissect the distinct and cell cycle-dependent functions of Snf2 Related CREBBP Activator Protein (SRCAP) and H2A.Z in gene regulation of pluripotent stem cells. We uncover dynamic changes of H2A.Z occupancy and continuous requirement of SRCAP over the cell cycle. We discover that SRCAP exhibits essential H2A.Z-independent functions in inhibiting DNA binding of dozens of pioneer transcription factors at enhancers by steric hindrance. In contrast, H2A.Z acts mainly as a transcriptional repressor gatekeeping the expression of lineage-specific genes. Our study establishes the catalytic-independent role of a chromatin remodeler in broadly regulating transcription factor binding, and demonstrates how a chromatin remodeler-histone variant pair orchestrates transcription to maintain self-renewal and plasticity of pluripotent stem cells.

Main text

Introduction

In Eukaryotes, most DNA is wrapped around nucleosomes made of histone octamers. While two copies of the four canonical histones make up most nucleosomes, histone variants can replace them in specific positions of the genome. H2A.Z is a highly conserved H2A histone variant essential for zygotic genome activation in drosophila and zebrafish and for post-implantation development in the mouse [1–3]. In vertebrates, there are two different isoforms of H2A.Z (H2A.Z.1 and H2A.Z.2) that differ by only 3 amino acids [4]. H2A.Z plays a central role in self-renewal and lineage commitment of multiple types of stem cells, including mouse

pluripotent stem cells (PSCs) [5–7]. Both Snf2 Related CREBBP Activator Protein (SRCAP) and Tip60/p400 remodeler complexes ensure H2A.Z deposition in mammals [8,9]. In mouse PSCs, H2A.Z deposition is mainly achieved by the SRCAP complex, made of the SRCAP protein bearing the catalytic ATPase activity and 9 other subunits [10]. The SRCAP complex binds to canonical nucleosomes and swaps the H2A-H2B dimer with a H2A.Z-H2B dimer [8]. It was also reported to facilitate the recruitment of some transcriptional regulators, but whether this function is independent of its role in depositing H2A.Z is unclear [11–13].

In PSCs, H2A.Z is broadly enriched at active and bivalent/poised promoters and enhancers [14,15]. H2A.Z has been proposed to regulate transcription at multiple levels, i.e. by modulating chromatin accessibility, repressing DNA methylation, altering transcription factor (TF) binding and enhancing RNA Polymerase II pausing [16–20]. H2A.Z nucleosomes protect shorter DNA segments compared to canonical nucleosomes, which was suggested to reflect nucleosome destabilization and to facilitate protein-DNA interactions [21].

Mechanistic understanding of transcriptional regulation by SRCAP and H2A.Z remains obscured by conflicting evidence and technical challenges. First, H2A.Z was reported to either increase or decrease both chromatin accessibility and TF binding [5,16,18,22,23]. Second, whether H2A.Z-containing nucleosomes are evicted or replaced with canonical nucleosomes when H2A.Z is depleted is unclear [5,24,25]. Thus, the specific function of H2A.Z with respect to H2A has not yet been addressed in vivo. Third, the proposed role of H2A.Z in inhibiting DNA methylation in mammals is only supported by weak evidence that is either correlative or uses slow H2A.Z knockdown approaches may cause indirect effects [26,27]. Fourth, depletion of H2A.Z causes genome-wide redistribution of the yeast SRCAP homolog (SWR1) [28], and nucleosomal H2A.Z inhibits human SRCAP binding [23], potentially leading to SRCAP-mediated changes in recruiting transcriptional regulators [29].

Here we dissect the direct and acute consequences of SRCAP loss and uncouple H2A.Z deposition from other SRCAP functions in transcriptional regulation. Our study reveals how SRCAP and H2A.Z coordinate their distinct functions to orchestrate gene regulation governing self-renewal and plasticity.

Results

Dynamic and cell cycle-dependent SRCAP-mediated H2A.Z positioning

To study the dynamics of H2A/H2A.Z exchange by SRCAP, we generated a CGR8 mouse embryonic stem cell (mESC) line allowing rapid degradation of the catalytic subunit of the SRCAP complex (SRCAP), using the auxin-inducible protein degradation system [30]. We knocked-in YPet-AID (YA) into the 3'end of both alleles of *srcap* and stably expressed the OsTir1 receptor to generate the SRCAP-Ypet-AID Tir1 (SYAT) cell line. We validated the pluripotency of SYAT cells by Alkaline Phosphatase assay and RT-QPCR of pluripotency TFs

(Fig.S1a), nuclear interphase localization and previously-described mitotic chromosome association of SRCAP [31] (Fig.S1b). CUT&RUN and CUT&TAG revealed SRCAP-YA enrichment at promoters and preferential colocalization with active transcription start sites (TSS) and H2A.Z peaks (Fig.S1c, S1d and 1a), as reported for SWR1 in yeast [28]. Upon addition of indole-3-acetic acid (IAA), SRCAP-YA was rapidly depleted (Fig.1b), and H2A.Z signal on mitotic chromosomes was decreased (Fig.S1e).

We then performed H2A.Z and H2A ChIP-seq (see Methods) at 2, 4, 6 or 8 hours after IAA addition. H2A.Z was depleted and replaced by H2A (Fig.1c and d) at 98% of H2A.Z ChIP-seq peaks, with the majority of peaks (72%) losing most H2A.Z within 2 h (Fig.S1f). H2A.Z turnover at regions specifically enriched for H2A.Z.1 or H2A.Z.2 (using data from [20]) was similar, suggesting a comparable impact of SRCAP depletion on H2A.Z.1 and H2A.Z.2 (Fig.S1g). The rate of SRCAP-mediated H2A.Z exchange was highest at active promoters, followed by active enhancers, and slightly slower at bivalent and poised enhancers (Fig.1e- f). The pace of H2A.Z loss was particularly fast at nucleosomes surrounding TSS of active genes (Fig.1g) and scaled with their transcriptional activity (Fig.S1h). Loci with the highest H2A.Z turnover were initially highly enriched for SRCAP, the SWI/SNF, NuRD and Ep400 chromatin remodelers, and several PSC TFs (Fig.1h and S1i), suggesting their role in H2A.Z turnover regulation. We next examined H2A.Z co-localization with the large number of regions depending on the pioneer TFs (pTFs) OCT4 and SOX2 for chromatin accessibility maintenance in PSCs [32,33]. H2A.Z was rapidly lost in these regions upon SRCAP depletion (Fig.S1j). Furthermore, knockdown of OCT4 (see Methods and [34]) rescued H2A.Z occupancy at OCT4-occupied regions (Fig.S1k), suggesting that OCT4 mediates H2A.Z eviction. These findings are in line with H2A.Z nucleosome eviction by the transcriptional machinery and gene regulatory factors [35,36].

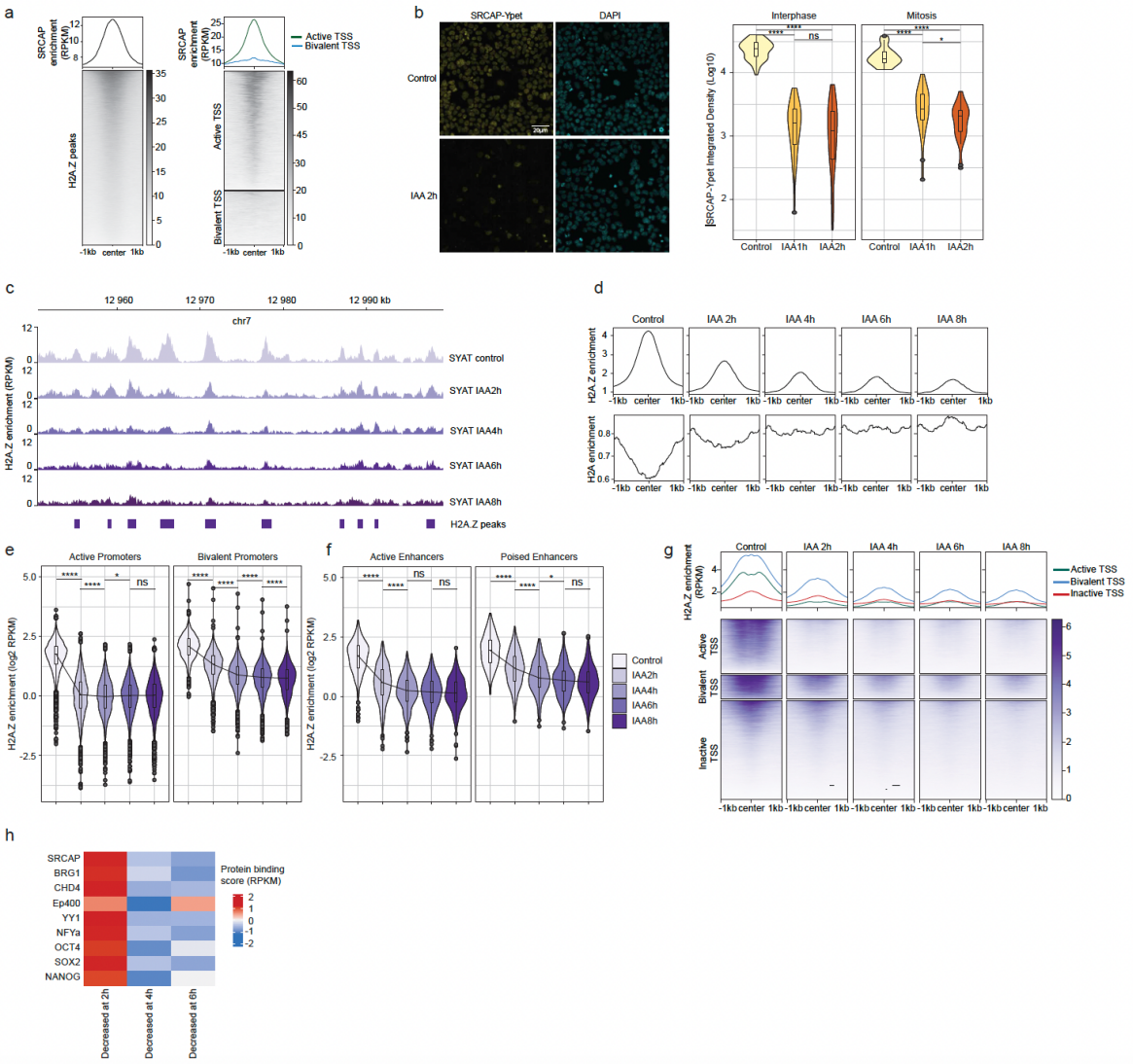

Fig.1: SRCAP degradation leads to rapid replacement of H2A.Z by H2A. **a**, SRCAP-YPet-AID genomic mapping by CUT&RUN at H2A.Z peaks (left panel) and active and bivalent TSS (right panel). **b**, Left panel: Microscopy snapshots of SYAT cells, treated with IAA or control for 2 h and stained with DAPI. Right panel: Quantification of total SRCAP-YA signal in interphase and mitotic cells treated with IAA or control. N = 50 cells per condition. **c**, Genome tracks of H2A.Z ChIP-Seq in SYAT cells treated with IAA. **d**, ChIP-Seq profiles of H2A.Z and H2A in SYAT cells treated with IAA. **e** and **f**, H2A.Z enrichment at active and bivalent promoters (**e**) and enhancers (**f**) upon SRCAP degradation. Black line: changes in median values. Boxes: interquartile range; dots: outlier points. **g**, ChIP-seq metaplots and heatmaps of H2A.Z enrichment around the TSS of active, bivalent, and inactive genes. **h**, Z-score enrichment of different DNA-binding proteins for the different H2A.Z turnover groups. p-values were determined by a pairwise Wilcoxon test, *: p<0.05, **: p<0.01, ***: p<0.001, ****: p<0.0001, ns: non-significant.

As TF binding, chromatin remodeler activity and transcriptional activity vary across the cell cycle, we determined H2A.Z positioning in early G1 (EG1), late G1 (LG1), S, G2/M phases, or mitosis (Methods and [33, 37]). Global variations of H2A.Z through the cell cycle were modest (Fig.2a) and H2A.Z was mostly located at active and bivalent/poised regulatory elements (Fig.2b). H2A.Z was lost at active promoters and enhancers at the mitosis-EG1 transition, but accumulated at bivalent and poised enhancers (Fig.S2a-b). We neither observed a mitotic shift of H2A.Z on the TSS nor a mitotic H2A.Z depletion at promoters as reported in different cell

types [38, 39], suggesting cell type-specificity of H2A.Z positioning. We then classified regulatory elements according to changes in H2A.Z occupancy between G2 phase and mitosis (Fig.2c and S2c). Global H2A.Z levels were equalized during mitosis at promoters and enhancers, in line with a quantitative resetting of the H2A.Z landscape before cells enter the next cell cycle (Fig.2d and S2d). Promoters in cluster 1 and cluster 3 showed enrichment for Gene Ontology (GO) terms associated with lineage specification and general cellular functions (Fig.S2e), respectively. Highly-expressed genes were more enriched in cluster 3 (Fig.2e), but enhancer activity levels were comparable in all enhancer clusters (Fig.S2f). Next, we performed ChIP-seq on the acetylated form of H2A.Z (acH2A.Z), associated with active regulatory elements and positively correlated with transcription levels [40]. Mitotic acH2A.Z levels were decreased in all three promoter clusters (Fig.2f and S2g, S2h), reflecting a shift in the equilibrium between acetylation and deacetylation during mitosis.

We next investigated SRCAP-dependent H2A.Z positioning during mitosis. We treated cells with IAA for 1 h and sorted asynchronous and mitotic cells depleted for SRCAP. 1 h IAA treatment decreased H2A.Z occupancy genome-wide (Fig.2g and S2i) at bivalent/poised promoters and enhancers in mitosis but not in interphase (Fig.2h and S2j). In contrast, 1 h IAA treatment in both mitosis and interphase decreased H2A.Z levels at active promoters and enhancers, in line with their high H2A.Z turnover rate (Fig.2h and S2j). This suggests that SRCAP-mediated H2A.Z turnover is accelerated in mitosis despite very low transcriptional activity [41], indicating transcription-independent mitotic H2A.Z eviction.

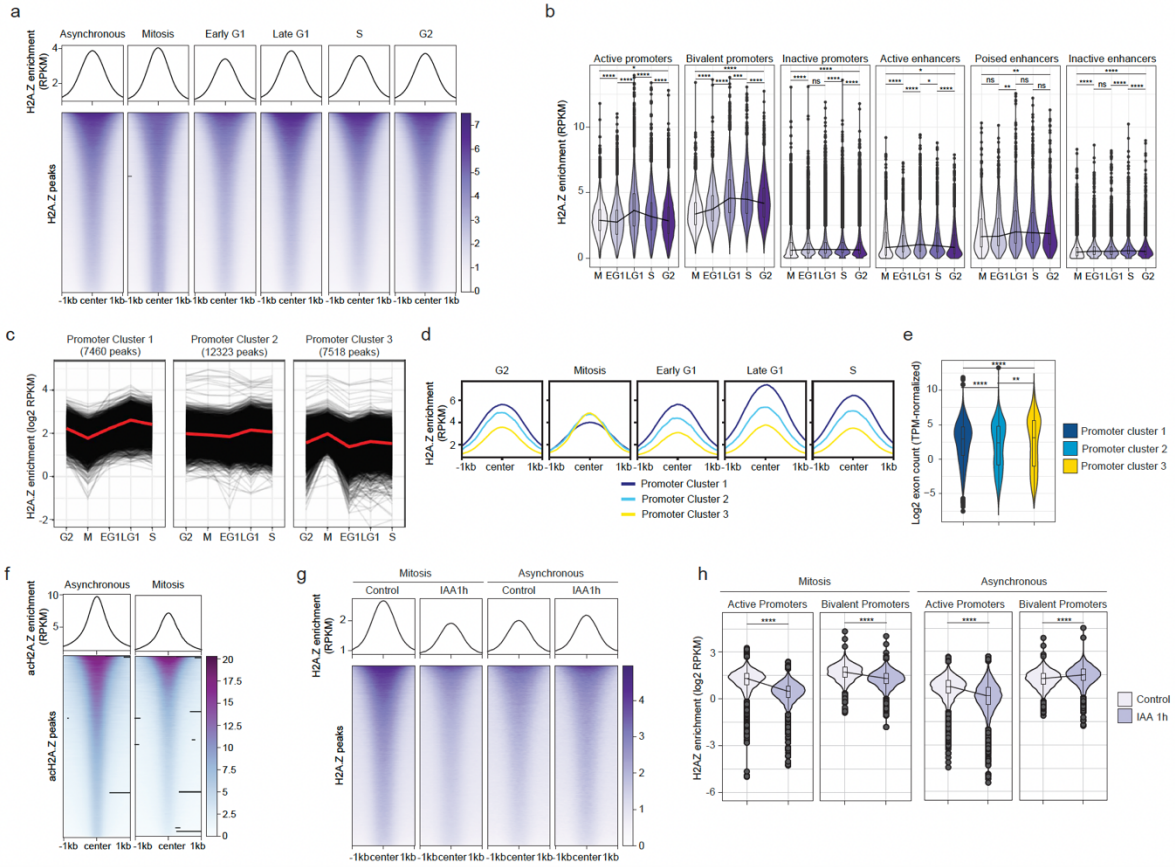

Fig.2: H2A.Z deposition across the cell cycle. a, Heatmaps and metaplots of H2A.Z enrichment centered on the summit of H2A.Z peaks across the cell cycle. **b**, H2A.Z enrichment across the cell cycle in promoters or enhancers, classified according to their activity. **c**, H2A.Z enrichment in promoter peaks in regions where mitotic H2A.Z was decreased, stable or increased with respect to G2 and EG1 phases. **d**, H2A.Z enrichment around H2A.Z peaks in the clusters shown in (**c**). **e**, Exon counts of genes regulated by each of the three promoter clusters. **f**, Heatmaps and metaplots of acH2A.Z enrichment centered on the summit of acH2A.Z peaks in asynchronous versus mitotic cells. **g**, Heatmap of H2A.Z enrichment centered on the summit of H2A.Z peaks in mitotic or asynchronous SYAT cells treated for 1 h with IAA. **h**, H2A.Z enrichment in promoters of mitotic or asynchronous SYAT cells treated for 1 h with IAA. p-values were determined by a pairwise Wilcoxon test, ****: $p<0.0001$, *: $p<0.05$, ns: non-significant.

SRCAP depletion unleashes the expression of master regulators of cell fate

We next performed nuclear RNA-seq after IAA treatment for 2, 4, 6 or 8 h in SYAT cells or wt CGR8 cells for 4 h to account for unspecific effects of IAA. We quantified both intronic reads, which accurately reflect acute transcriptional activity [42], and exonic reads. In wt CGR8 cells, 4 h of IAA treatment did not impact transcription (Fig.S3a). In SYAT cells, changes in intronic reads were already apparent after 2 h and peaked after 6 h of IAA treatment, with 211 and 276 genes up- and downregulated, respectively (Fig.3a and Table S1). Mature transcripts were more gradually affected starting from 2 h of IAA treatment (Fig.S3b). These results contrast with H2A.Z knockdown in mESCs, which mainly results in upregulated genes [20,43] that poorly overlap with the genes we identified (Fig.S3c). The pace of H2A.Z removal was comparable between transcriptionally-affected and unaffected genes (Fig.S3d). Bivalent genes were markedly over-represented among upregulated genes upon SRCAP depletion (Fig.3b), but no

functional gene category was overrepresented in downregulated genes (Fig.S3e). Upregulated genes were highly enriched in DNA-binding proteins, notably in lineage-specific transcription factors (Fig.3c and S3f). Among those were TFs associated with differentiation towards germ layers, especially mesoderm (Gata3, Gata6, BMP4, Meis1, Lefty2), or with pluripotency maintenance (Nanog, Myc, Trim28, Zfp42) (Fig.S3g, Table S1). In contrast, downregulated genes were enriched in ubiquitously expressed genes (Fig.3d). We next quantified the number of promoter-enhancer loops formed for each gene (Methods). Upregulated genes formed more promoter-enhancer loops than downregulated genes (Fig.3e), in line with enhancer-dependent regulation of lineage-specific genes [44]. We then quantified changes in the proteome of the 4h IAA-treated cells by Mass Spectrometry (Methods). Only 52 and 30 proteins were significantly increased and decreased in their levels, respectively (Fig.3f, Table S2). GO terms associated with DNA binding and transcriptional regulation were enriched in upregulated proteins (Fig.S3h), in line with upregulated mRNAs.

We next investigated the impact of mitotic SRCAP depletion on gene reactivation during EG1 (Methods). We treated cells with IAA for 1 h, followed by sorting of EG1 cells or LG1 cells (undergoing SRCAP depletion during mitosis and G1, respectively). Mitotic SRCAP depletion resulted mainly in downregulation of genes in EG1 (Fig.3g), many of which were housekeeping genes (Fig.S3i). In contrast, SRCAP depletion during G1 resulted in a smaller number of downregulated genes (Fig.3h). This suggests that SRCAP activity during mitosis and at mitotic exit is mainly required for transcriptional reactivation in early G1.

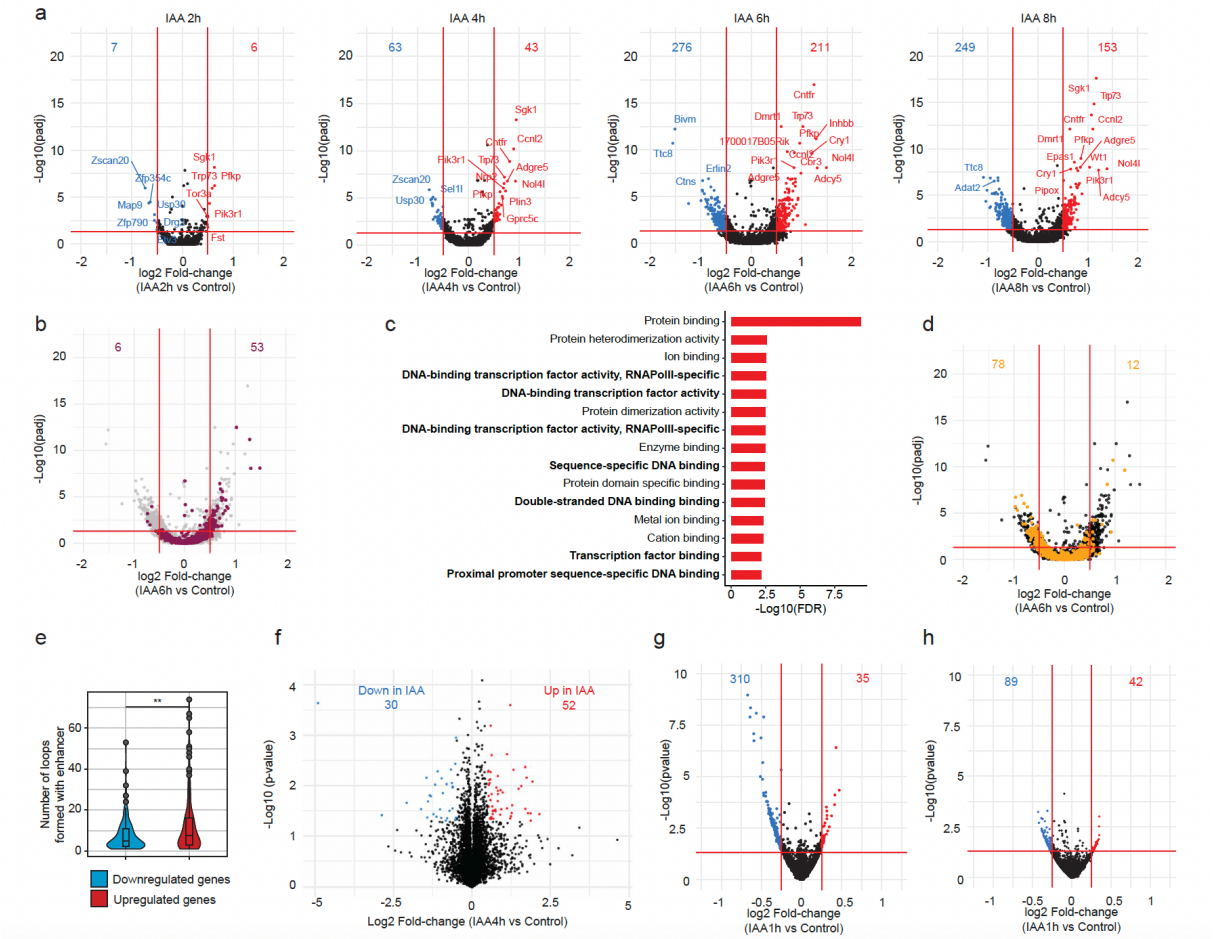

Fig.3: SRCAP degradation leads to transcriptional deregulation. a, Fold-change of intronic reads and adjusted p-value for SYAT cells treated for 2, 4, 6 and 8 h with IAA. Numbers: genes significantly downregulated (blue) or upregulated (red) with a threshold of |log2FC|>0.5 and adjusted p-value < 0.05. **b**, Fold-change of intronic reads and adjusted p-value for SYAT cells treated for 6 h with IAA. Genes regulated by a bivalent promoter are colored. **c**, Top 15 GO terms enriched for genes upregulated at 6 h with the category "molecular function". **d**, Fold-change of intronic reads and adjusted p-value for SYAT cells treated for 6 h with IAA. Ubiquitously-expressed genes are colored. **e**, Number of promoter-enhancer loops formed for genes found to be downregulated or upregulated at any time point. p-values were determined by a pairwise Wilcoxon test, **: p<0.01. **f**, Changes in proteome composition in SYAT cells treated with IAA for 4 h compared to control. Numbers: proteins enriched (blue) or depleted (red) from the proteome upon IAA treatment with a threshold of |log2FC|>0.5 and p-value < 0.05. **g** and **h**, Fold-change of intronic reads, for SYAT cells treated for 1 h with IAA and sorted in EG1 (**g**) or LG1 (**h**). Numbers: genes significantly downregulated (blue) or upregulated (red) with a threshold of |log2FC|>0.25 and p-value < 0.05.

SRCAP depletion alters histone modifications and nucleosome properties

To understand the mechanisms underlying changes in transcriptional activity upon SRCAP depletion, we analyzed changes in histone post-translational modifications by ChIP-seq and nucleosome properties by MNase-seq. At 4 h of IAA, H3K4me3 levels were down in 66.6% of H3K4me3-enriched regions, with a marked decrease at bivalent promoters (Fig.4a-b and S4a). This is in line with the role of H2A.Z in recruiting SET1/COMPASS complexes [5], which allows H3K4me3 maintenance [45]. Changes in H3K4me3 enrichment at +1 nucleosomes were mildly correlated with transcriptional changes for both active and bivalent genes (Fig.4c and S4b),

and promoters of downregulated genes displayed a more pronounced decrease of H3K4me3 (Fig.S4c), in line with the role of H3K4me3 in fostering transcriptional activity [46,47].

H3K27me3 levels decreased at 27.6% of regions (4799 peaks) and increased at 19.6% of regions (3402 peaks), including at bivalent promoters (Fig.4a, d and S4d). H2AK119ub1 displayed a massive increase at most enriched loci (52.6%, 20881 peaks), especially at bivalent promoters (Fig.4a, e and S4e). Therefore, changes in H3K27me3 and H2AK119ub1 levels do not explain transcriptional changes at bivalent genes.

We next performed MNase-seq using high or low concentrations of MNase (Methods) on SYAT cells treated with control or IAA for 4 h. We classified nucleosomes in four classes according to initial H2A.Z enrichment scores. H2A.Z enrichment scaled with nucleosome occupancy at regulatory elements (Fig.4f and S4h). However, this coupling was also observed upon SRCAP/H2A.Z depletion, suggesting that nucleosome occupancy is not primarily regulated by H2A.Z but is mostly dependent on the genomic context. The size of nucleosome-protected fragments increased upon SRCAP degradation independently of initial H2A.Z levels in regions containing these nucleosomes (Fig.4g and S4i). While agreeing with the reported unwrapped state of H2A.Z nucleosomes [21], this also raises the possibility that SRCAP unwraps nucleosomes independently of H2A.Z deposition, similarly to SWR1 in vitro [48,49]. We then focused on fragile nucleosomes, defined by a high signal ratio between MN-low versus MN-high digestion and enriched around TSS and TF binding sites [50,51]. Nucleosome fragility scaled with H2A.Z levels at active and bivalent regulatory regions (Fig.4h and S4j), in agreement with reported H2A.Z enrichment in fragile nucleosomes [52–54]. Surprisingly, IAA did not induce a global decrease of nucleosome fragility (Fig.4h and S4j). Furthermore, nucleosome fragility was unchanged at +1 nucleosomes of downregulated genes and increased at upregulated genes (Fig.S4k), suggesting that fragility depends on the genomic context but not on H2A.Z occupancy. Therefore, alteration of nucleosome properties does not explain the transcriptional changes mediated by SRCAP depletion.

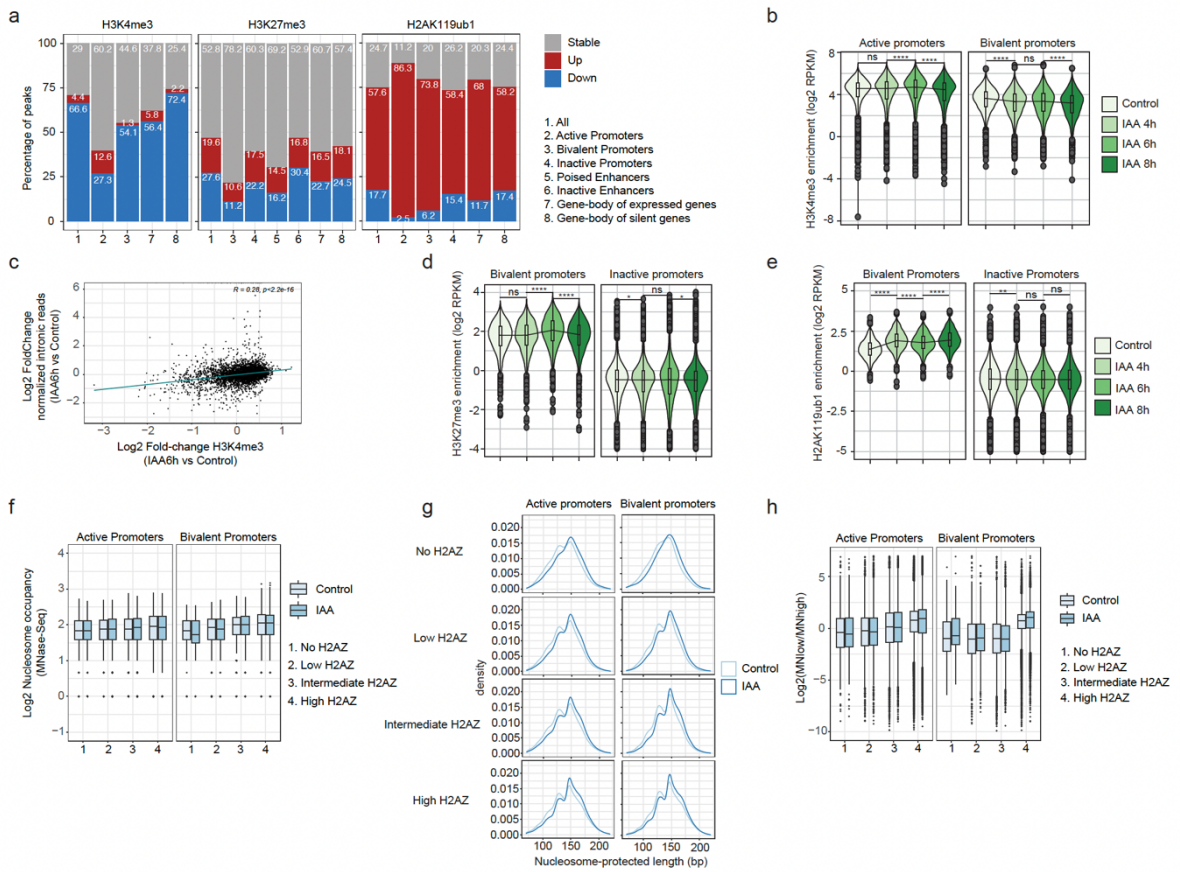

Fig.4: Impact of SRCAP/H2A.Z loss on nucleosome properties and post-translational modifications. a, Percentage of different types of genomic regions with increased, stable or decreased H3K4me3, H3K27me3 and H2AK119ub1 marks. **b**, H3K4me3 enrichment at active and bivalent promoters, in SYAT cells treated with control or IAA for 4, 6 and 8 h. **c**, Scatterplot of intronic reads of genes controlled by active promoters as a function of H3K4me3 enrichment changes between 6 h of IAA treatment and control. Upper right corner: Pearson correlation coefficient. **d** and **e**, H3K27me3 (**d**) and H2AK119ub1 (**e**) enrichment at bivalent and inactive promoters in SYAT cells treated with control or IAA for 4, 6 and 8 h. **f**, Nucleosome occupancy at promoters in SYAT cells as a function of H2A.Z levels, in control or after 4 h of IAA treatment. **g**, MNase-Seq fragment densities in SYAT cells treated with control or IAA for 4 h, as a function of H2A.Z enrichment and the class of promoter where nucleosomes are localized. **h**, Fragile nucleosomes in nucleosomes of different types of promoters, as a function of H2A.Z levels. p-values were determined by a pairwise Wilcoxon test; ****: p<0.0001; ***: p<0.001; **: p<0.01; *: p<0.05, ns: non-significant.

SRCAP depletion unleashes transcription factor binding

We next performed ATAC-seq after treating SYAT cells for 2, 4, 6 or 8 h with IAA. Overall chromatin accessibility was unchanged within the first 6 h of SRCAP degradation (Fig.S5a). Promoters were mostly unaffected in their accessibility, while many distal intergenic regions displayed increased or decreased accessibility (Fig.5a-b). To understand the mechanisms underlying these changes, we analyzed TF footprints in accessible regions using the TOBIAS bioinformatic pipeline [55]. In wt CGR8 cells, a 4 h IAA treatment had an anecdotal impact on TF footprinting (Fig.S5b, Table S3). In SYAT cells, hundreds of TF motifs already displayed significant changes in footprinting after 2 h of IAA treatment, and these alterations were very consistent across time points (Fig.5c and S5c). About four times more motifs had their footprints enriched (up motifs) than depleted (down motifs) at all time points after IAA treatment

(Fig.5c and S5c). Up and down motifs were mostly located in distal regulatory regions and promoter regions, respectively (Fig.5d and S5d). As promoter- and enhancer-regulated genes tend to be downregulated and upregulated upon SRCAP/H2A.Z depletion, respectively (Fig.3e), this suggests that changes in TF binding could contribute to transcriptional changes caused by SRCAP depletion. We next asked whether the predominant transcriptional downregulation after mitotic IAA treatment (Fig.3g) could be caused by a shift towards more downregulated TF footprints. We performed 1 h of IAA or control treatment, and sorted cells enriched for the end of M-phase (see Methods) and in EG1 to perform ATAC-seq prior to and concurrently to EG1 transcriptional changes, respectively. Changes in TF footprinting were more pronounced for down relative to up motifs as compared to longer IAA treatments in asynchronous cells (Fig.5e), in line with transcriptional downregulation upon mitotic SRCAP/H2A.Z loss.

As pTFs can bind nucleosomal DNA, we reasoned that their binding might be particularly sensitive to nucleosome composition. We quantified the number of pTFs enriched in up vs downregulated motifs, using a classification of pTFs based on [56,57] (see Methods). 87 out of 376 up-TFs (23.1%) but only 7 out of 97 (7.2%) down-TFs after 4 h of IAA treatment were known pTFs (Fig.S5e). Therefore, pTF binding is generally impaired by the presence of SRCAP and/or H2A.Z.

To gain a broader view of changes in protein-DNA interactions induced by SRCAP depletion, we treated cells with IAA for 4 h and analyzed changes in proteins bound to chromatin (chromatome) ([58] and Methods). We found 174 proteins significantly up or downregulated. In line with TOBIAS analysis, more TFs were upregulated than downregulated (Fig.5f). TF protein levels were unaffected (Fig.3f and Table S2), suggesting that changes in TF binding are not mediated by changes in their concentrations. In contrast to SRCAP, H2A.Z was only slightly decreased in the whole chromatome (Fig.5f and Table S2), suggesting low or SRCAP-independent H2A.Z turnover in regions that are not recovered in ChIP-seq experiments, such as sonication-resistant heterochromatin [59].

We then performed ChIP-seq on selected TFs with altered footprints and/or enrichment in the chromatome. 28.2% of OCT4 and 42% of SOX2 binding sites were more occupied upon IAA treatment, in line with TOBIAS and chromatome analysis (Fig.5g and h). However, OCT4 was shown to bind H2A.Z nucleosomes [60] and to lose binding upon H2A.Z knockdown [5]. Accordingly, sites bound by OCT4-only lost binding upon H2A.Z swapping with H2A, in contrast to sites bound by both OCT4 and SOX2 (Fig.S5f), in line with SOX2-dependent OCT4 binding on canonical nucleosomes [61,62]. Furthermore, SOX2 knockdown (Methods, [63]) decreased the number of OCT4 binding sites, and the remaining bound sites were highly enriched for H2A.Z (Fig.S5g). Therefore, without SOX2, OCT4 favors binding to H2A.Z over H2A nucleosomes, also explaining the largely intact pioneer activity of OCT4 in the absence

of SOX2 [33]. NANOG, YY1 and NFY-a also displayed altered genome occupancy in line with TOBIAS and/or chromatome analysis (Fig.5g), and OCT4, SOX2 and NANOG sites displayed increased binding in distal regulatory regions (Fig.S5h).

Since changes in TF binding were already maximal 2 h after IAA addition (Fig.S5c), we reasoned that TFs could drive subsequent changes in chromatin accessibility (Fig.5a). Loss and gain of TF binding were associated with corresponding changes in chromatin accessibility (Fig.5i), in line with the high number of pTFs with increased footprints (Fig.S5e). Furthermore, loci with increased OCT4 or SOX2 binding displayed more pronounced increased accessibility than loci with stable or decreased binding (Fig.S5i). This suggests that alterations in pTF binding drive changes in chromatin accessibility upon SRCAP/H2A.Z depletion.

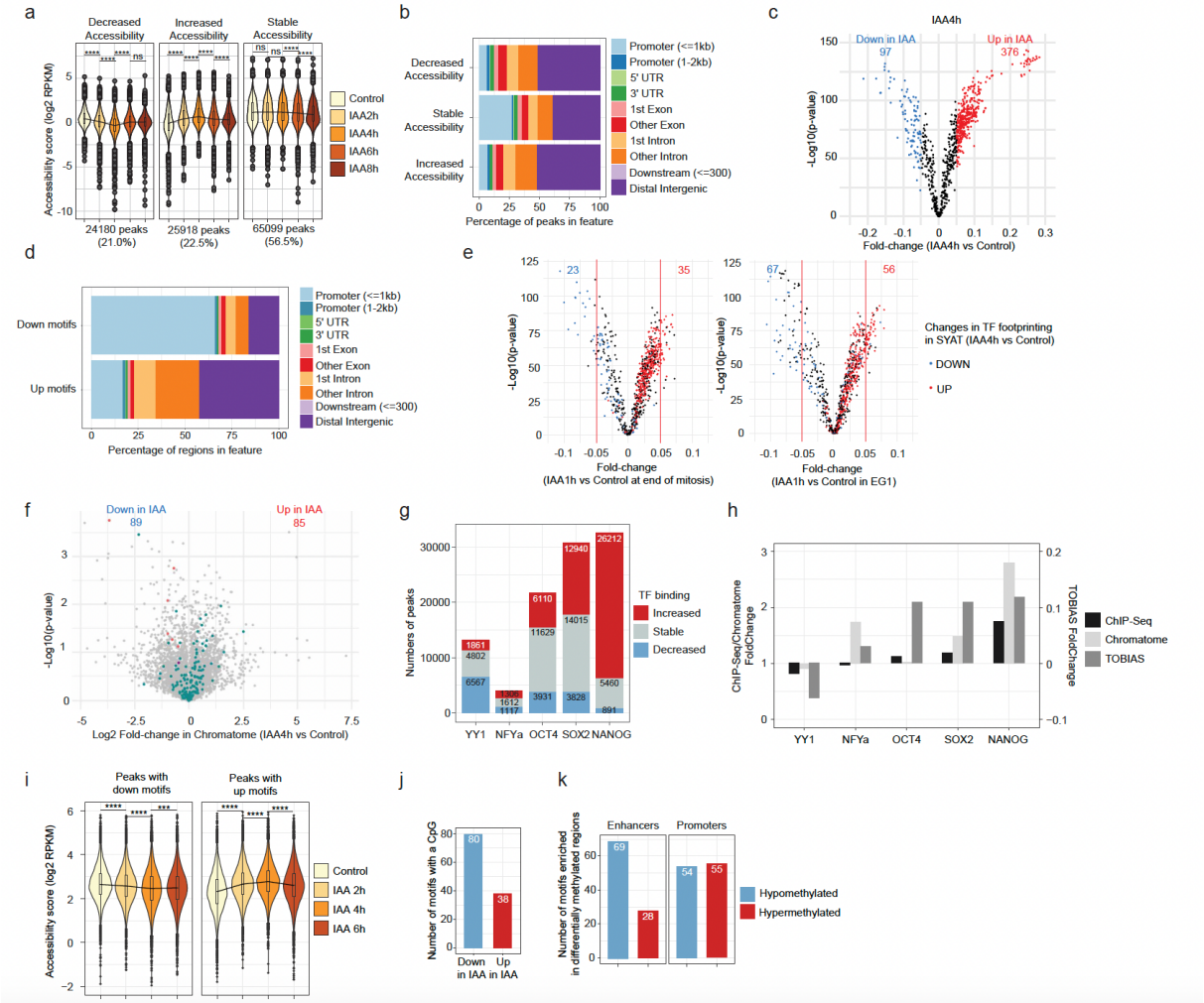

Fig.5: SRCAP depletion alters transcription factor binding. **a**, Chromatin accessibility changes in SYAT cells treated with control or IAA for 2, 4, 6 and 8 h. **b**, Percentage of different types of genomic regions in accessible regions belonging to accessibility classes defined in (a). **c**, Fold-change of TF footprinting calculated using TOBIAS in SYAT cells treated 4 h with IAA versus control. Numbers: TF motifs predicted to lose (blue) or gain (red) binding upon IAA treatment with a threshold of |FC|>0.05 and p-value < 0.0001. **d**, Percentage of occurrence of all motifs, for TFs predicted to gain or lose binding in SYAT cells upon IAA treatment, for different types of genomic regions. **e**, Fold-change of TF footprinting calculated using TOBIAS in SYAT cells at the end of mitosis (left panel) or EG1 (right panel). Numbers: TF motifs predicted to lose (blue) or gain (red) binding upon IAA treatment with a threshold of |FC|>0.05 and p-value < 0.0001. Colors: Predicted TF footprinting changes in SYAT treated 4 h with IAA versus control. **f**, Chromatome analysis. Turquoise: TFs; red: members of SRCAP complex; purple:

H2A.Z. Numbers: proteins enriched (blue) or depleted (red) from the chromatome upon IAA treatment with a threshold of |log2FC|>0.5 and p-value < 0.05. **g**, Numbers of peaks with an increased or decreased TF ChIP-seq enrichment after 4 h of IAA treatment in SYAT cells. **h**, Fold-change in TF binding determined by ChIP-Seq, chromatome and TOBIAS prediction analysis. **i**, Chromatin accessibility changes upon IAA treatment for TF motifs predicted to gain or lose binding. **j**, Number of motifs containing at least one CpG, in motifs predicted by TOBIAS to lose or gain binding upon SRCAP depletion. **k**, Numbers of motifs significantly enriched in H2A.Z peaks located in promoters or enhancers and displaying cytosine hyper- or hypomethylation upon SRCAP/H2A.Z loss. p-values were determined by a pairwise Wilcoxon test; ****: p<0.0001; ***: p<0.001; ns: non-significant.

DNA methylation changes do not explain changes in TF binding upon SRCAP depletion

Since H2A.Z was proposed to antagonize DNA methylation [26,64], we reasoned that SRCAP loss may increase DNA methylation, which could subsequently mediate changes in TF binding. CpGs were over-represented in down vs up motifs (Methods and Fig.5j), and TFs with decreased footprints included methyl-sensitive NRF1 and ZBTB33 [65,66] (Table S3).

We quantified changes in DNA methylation at H2A.Z-occupied loci after 4 h of IAA treatment using Enzymatic Methyl Sequencing (EM-seq). Global DNA methylation displayed only minor changes (Fig.S5j). While some regulatory elements displayed increased or decreased CpG methylation upon IAA treatment (Fig.S5k), their accessibility was unaffected (Fig.S5l). Next, we treated SYAT cells with the GSK-3484862 DNMT1 inhibitor for 5 days, which decreases DNA methylation by 80% in PSCs [67] and performed ATAC-seq after 4 h of IAA or control treatment. DNMT1 inhibition only slightly dampened the impact of IAA on increased TF footprints and did not impact decreased TF footprints (Fig.S5m), suggesting that changes in DNA methylation plays a minor role in regulating TF binding. To determine if TF binding changes could lead to changes in DNA methylation, we identified enriched TF binding motifs in hyper- and hypomethylated H2A.Z peaks at promoters and enhancers. Many TF motifs were enriched in hypomethylated enhancers (Fig.5k). Our results suggest that acute changes in DNA methylation are mainly secondary to TF activity and play a minor role in further enhancing TF binding at hypomethylated motifs.

SRCAP and H2A.Z have distinct, complementary roles in transcriptional regulation

To determine H2A.Z-independent functions of SRCAP, we generated a catalytically-dead SRCAP protein (cdSRCAP) deficient for H2A.Z deposition by mutating 3 amino acid residues in its ATPase domain (Fig.S6a). We then engineered the SYAT cell line for doxycycline (dox)-inducible expression of either wtSRCAP or cdSRCAP fused to mCherry (Methods), hereafter referred to as wtSRCAP and cdSRCAP cell lines. We induced expression of wtSRCAP-mCherry or cdSRCAP-mCherry for 24 h, and treated cells with IAA or control for 4 h. We FACSorted cells with the same average mCherry fluorescence to ensure identical expression levels of wt and cdSRCAP and performed ChIP-seq for H2A.Z (Fig.6a). cdSRCAP cells displayed lower global H2A.Z enrichment than wtSRCAP cells (Fig.S6b), and H2A.Z levels

were rescued within <10% of the control condition at 44,769 peaks in wtSRCAP but not cdSRCAP cells (see Methods) (Fig.6b).

We then compared transcriptional changes in IAA-treated cells expressing wtSRCAP or cdSRCAP. wtSRCAP compensated transcriptional changes mediated by endogenous SRCAP degradation more than cdSRCAP (Fig.S6c). We clustered genes with intronic counts significantly differing between any pair of samples, according to their changes as a function of H2A.Z and SRCAP levels in wtSRCAP or cdSRCAP cells (Fig.6c). Genes in clusters A and B were negatively regulated by H2A.Z, while genes in clusters D and E were positively regulated by SRCAP. Clusters C and F reflected conflicting effects of H2A.Z and SRCAP on gene regulation, resulting in no significant differences in expression upon SRCAP degradation in SYAT cells (Fig.6d). Genes upregulated by SRCAP (clusters D and E) were associated with a general cellular function GO term (Fig.S6d) and included 70 housekeeping genes, indicating an H2A.Z-independent role of SRCAP in activating ubiquitously-expressed genes. H2A.Z played a dominant role in transcriptional repression of lineage-specific genes, confirmed by direct comparison of cdSRCAP versus wtSRCAP-expressing cells in both control and IAA conditions (Fig.6e-f and Fig.S6e-f). We next asked whether the H2A.Z-independent SRCAP function in stimulating transcription is determinant for gene reactivation at mitotic exit. Affected genes from all clusters stimulated by SRCAP were downregulated upon IAA treatment (Fig.6g). In contrast, 1 h-IAA treatment in LG1 cells led to transcriptional changes closer to those of longer IAA treatments in asynchronous cells (Fig.S6g). This suggests that transcriptional reactivation at mitotic exit is dominated by the stimulatory effect of SRCAP, and that the inhibitory role of H2A.Z comes into play only later during G1 phase.

We then performed ATAC-seq after 24 h of dox and 4 h of IAA treatment in wtSRCAP and cdSRCAP cell lines. Overall changes in chromatin accessibility upon IAA treatment were minor and comparable in both cell lines (Fig.S6h). Changes in chromatin accessibility caused by SRCAP depletion were abolished upon wtSRCAP but also cdSRCAP overexpression (Fig.S6i), suggesting that these are mostly H2A.Z-independent. We then used TOBIAS to analyze TF footprints in the wtSRCAP or cdSRCAP cell lines in control or IAA conditions. K-mean clustering of TF footprinting scores yielded 6 clusters displaying different dependencies to SRCAP and/or H2A.Z levels (Fig.6h). We identified two clusters with a predominant role of SRCAP in increasing (cluster 1) or decreasing (cluster 2) TF binding (Fig.6i), as well as a role for H2A.Z in positive (cluster 3 and 4) or negative regulation (cluster 5) of TF binding at hundreds of motifs (Fig.6i). Overall, SRCAP strongly prevented TF association with their motifs while H2A.Z had both enhancing and inhibitory effects on TF binding (Fig.6j). We then compared TF footprinting in rescued peaks in wtSRCAP cells treated with control or IAA, allowing us to determine the impact of different SRCAP levels on TF footprinting independently of H2A.Z levels. Both up and down motifs overlapped substantially with those identified upon

IAA treatment of SYAT cells, confirming the prominent H2A.Z-independent role of SRCAP in regulating TF binding (Fig.S6j). SRCAP and to a lesser extent H2A.Z tended to hinder TF binding at distal regulatory elements, as seen from the mostly distal localization of the TF motifs in clusters 2 and 5 (Fig.S6k). Conversely, both SRCAP and H2A.Z tended to stimulate TF binding at promoters, as seen from the larger fraction of TF motifs located in promoters in their main activatory clusters 1 and 4 (Fig.S6k). In addition, SRCAP strongly disfavored pTF association with their motifs (112 SRCAP- vs 5 SRCAP+ motifs) (Fig.S6l). Taken together, this suggests that H2A.Z-independent activity of SRCAP plays a major role in restricting pTF binding.

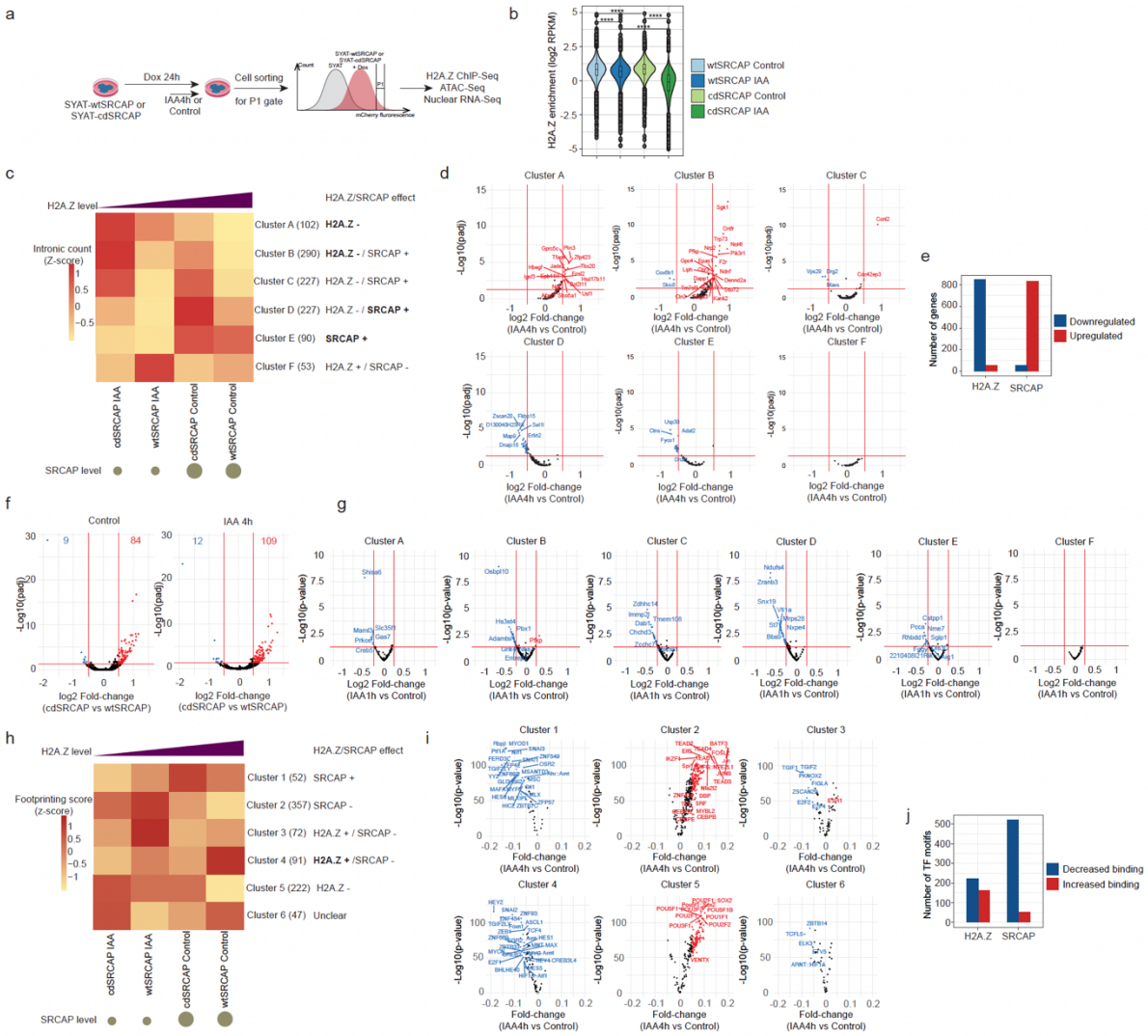

Fig.6: H2A.Z-dependent and independent functions of SRCAP. a, Experimental procedure for dox-induced wtSRCAP and cdSRCAP expression and cell sorting. **b**, H2A.Z enrichment in rescued peaks upon overexpression of wtSRCAP or cdSRCAP treated with control or IAA for 4 h. **c**, Heatmap of normalized intronic read counts ranked according to H2A.Z and SRCAP levels and k-mean-clustered. When SRCAP and H2A.Z display opposite effects, the dominant effect is written in bold. **d**, Fold-change of intronic reads and adjusted p-value for SYAT cells treated 4 h with IAA versus control, in the six gene clusters determined in (**c**). Colored dots: genes significantly downregulated (blue) or upregulated (red) with a threshold of |log2FC|>0.5 and adjusted p-value < 0.05. **e**, Numbers of genes downregulated or upregulated by H2A.Z or SRCAP. **f**, Fold-change of intronic reads between cdSRCAP and wtSRCAP and adjusted p-value in control (left) or IAA condition (right). Numbers: genes significantly lower (blue)

or higher (red) in cdSRCAP with a threshold of |log2FC|>0.5 and adjusted p-value < 0.05. **g**, Fold-change in intronic reads in the 6 clusters defined in (c) for SYAT cells treated for 1 h with IAA or control and sorted in EG1. **h**, Heatmap of TOBIAS footprinting scores ranked according to H2A.Z and SRCAP levels and k-mean-clustered. When SRCAP and H2A.Z display opposite effects, the dominant effect is indicated in bold. **i**, Fold-change of TF footprinting calculated using TOBIAS in SYAT cells treated 4 h with IAA versus control for the six clusters determined in (**h**). Colored dots: TF motifs predicted to lose (blue) or gain (red) binding upon IAA treatment with a threshold of |FC|>0.05< 0.0001. **j**, Numbers of TF motifs with binding increased or decreased by H2A.Z or SRCAP.

SRCAP inhibits TF binding by steric hindrance

The catalytically-independent inhibition of TF binding mediated by SRCAP could be caused by physically blocking the access of TFs to their binding sites (steric hindrance) and/or by decreasing TF affinity for their binding sites through chemical modification of chromatin or physical mechanisms acting through deformation of the DNA double-helix [68,69]. Several arguments favor a steric hindrance mechanism. First, the SRCAP complex covers a large fraction on the nucleosome [70–73]. Using a published structure [70], we computed the surface of DNA accessible to molecules considering either DNA in a free or SRCAP complex-bound nucleosome. For TFs (approximated as pseudo-spheres with radii of 20-30 Å [74,75]), DNA was 2-3-fold less accessible on SRCAP-bound nucleosomes (Fig.7a). Second, SWR1 complexes remain bound to nucleosomes in vitro for several minutes [49,76]. When crossing our SRCAP mapping and MNase data, we found that nucleosomes and SRCAP peaks were strongly colocalizing (Fig.S7a), confirming that SRCAP mostly occupies nucleosomal DNA in vivo. Third, the motifs of TFs increasing their binding upon SRCAP loss (cluster 2 in Fig.6) colocalize with SRCAP (Fig.S7b). NANOG, which strongly increased its binding upon SRCAP depletion (Fig.5g-h), displayed maximal SRCAP enrichment at the center of its ChIP-seq peaks (Fig.7b). Fourth, we reasoned that a steric hindrance mechanism implies its immediate mitigation after SRCAP degradation. After 2 h of IAA treatment, changes in TF footprinting were already maximal (Fig.S5c). Furthermore, NANOG ChIP-seq after 2 h of treatment with different doses of IAA (Fig.S7c and d) also revealed increased NANOG occupancy in regions initially co-occupied by SRCAP (Fig.7c).

However, these results do not fully exclude that SRCAP loss may induce rapid changes in local chromatin chemistry or physical properties, which could alter TF binding affinity. The genomic occupancy of TFs depends both on their binding frequency and residence time on specific sites. While alterations of chemical or physical properties of chromatin would alter TF residence time, steric hindrance is expected to decrease TF binding frequency by hiding TF binding sites. To discriminate between these scenarios, we determined the impact of SRCAP on DNA-binding dynamics of NANOG using single-molecule fluorescence tracking (SMT) in live cells (Fig.7d). We expressed a Halo-NANOG fusion protein at low levels in SYAT cells, cdSRCAP cells – dox, cdSRCAP + dox and wtSRCAP + dox (Methods). We first determined the overall bound fraction of dye-labeled Halo-NANOG by tracking molecules at 85Hz [77]. We

analyzed the distribution of molecular frame-to-frame jump distances with a multi-component diffusion model[78] (Fig.S7e,f), which revealed a higher bound fraction of NANOG in the absence of SRCAP (Fig.S7g and Methods). This increase in bound fraction was counteracted by expression of wt or cdSRCAP (Fig.S7h-j). Next, we determined the spectrum of residence times of Halo-NANOG by tracking bound molecules at 0.5Hz using several time-lapse conditions [79] (Fig.S7k and Methods). We then focused our analysis on molecules binding longer than 50s, which are mostly specifically-bound molecules. As expected, the fraction of long-binding molecules was increased in absence of SRCAP, and this effect was suppressed by expression of wt or cdSRCAP (Fig.7e, Fig.S7m). From the bound fractions and residence times, we calculated the binding frequencies using a kinetic model including diffusing, transiently binding, and stably binding NANOG molecules [80,81] (Fig.S7l and Methods). Strikingly, the binding frequency of NANOG increased four-fold upon SRCAP degradation, and this effect was suppressed by expression of wt or cdSRCAP (Fig.7f, Fig.S7n). Interestingly, NANOG residence time was decreased upon SRCAP depletion, (Fig.S7o), in line with the extension of the NANOG binding landscape to lower affinity regions displaying low accessibility and OCT4/SOX2 occupancy (Fig.S7p). These results indicate that increased binding frequency of NANOG drives increased NANOG binding upon SRCAP depletion, in line with SRCAP inhibition of TF binding by steric hindrance.

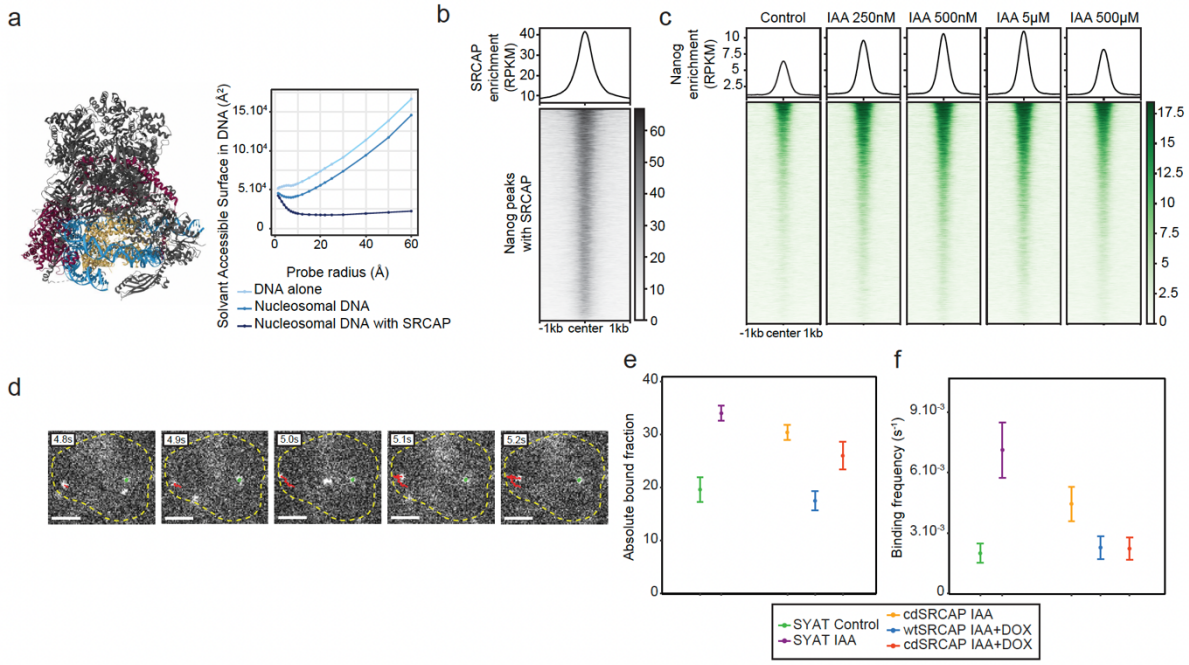

Fig.7: SRCAP decreases NANOG binding by steric hindrance. a, Left panel. Cryo-EM structure of human SRCAP determined by Yu et al. [70] , DNA is displayed in blue, histones in yellow, SRCAP subunit in purple and all other subunits of the SRCAP complex in grey. Right panel. Surface of the DNA accessible to molecules of different radii calculated from the Cryo-EM structure. **b,** SRCAP enrichment determined by CUT&RUN, centered on NANOG peaks where SRCAP peaks are also detected. **c,** Nanog enrichment at binding sites of both NANOG and SRCAP in SYAT cells treated with different doses of IAA for 2 hours. **d,** Images of single Halo-NANOG molecules in a cell nucleus at indicated time points, and corresponding tracks (colored). Scale bar: 3 µm. **e,** Absolute fraction of Halo-NANOG molecules bound longer than 50s, calculated from data displayed in fig.S7-g,j,l,n, with the statistics provided there. Data are represented as calculated values ± error from error propagation. **f,** Binding frequency of Halo-NANOG molecules calculated from data displayed in fig.S7-f,g,i,j,l,n, with the statistics provided there. Data are represented as calculated values ± error from error propagation.

Discussion

The transient nature of most DNA-protein interactions is well-established in mammalian systems [82–84]. However, the direct, acute impact of these interactions on chromatin structure and composition is more challenging to characterize. Several studies reported that the recruitment and nucleosome-remodeling activity of the BAF complex occur continuously on a time scale of minutes [33,85,86]. Here we demonstrate dynamic SRCAP-mediated H2A.Z turnover over active and bivalent/poised regulatory elements on similar time scales. The SRCAP-dependent H2A.Z turnover rates at promoters correlating with transcriptional activity is in line with transcription-mediated eviction of full H2A.Z nucleosomes or H2A.Z-H2B dimers [36,87–90], followed by rapid re-incorporation of H2A-H2B and SRCAP-mediated loading of H2A.Z-H2B. The fact that SRCAP binds preferentially to canonical nucleosomes [23] and the correlation of its genomic occupancy with H2A.Z turnover rates (Fig.1a, h) suggest that the pace of nucleosome eviction sets the rate of SRCAP recruitment to chromatin. Surprisingly, SRCAP-mediated H2A.Z turnover is even faster during mitosis than interphase, despite very low mitotic transcriptional activity [41]. This suggests that SRCAP maintains H2A.Z levels on mitotic

chromosomes by competing with transcription-independent H2A.Z eviction mechanisms that remain to be identified.

Despite the initial characterization of SRCAP for its ability to recruit transcriptional coactivators [11–13], its role in gene regulation has become increasingly viewed through the lens of its H2A.Z deposition activity. Our study clarifies the specific and direct functions of SRCAP and H2A.Z in gene regulation. We found no evidence that H2A.Z is directly involved in nucleosome destabilization or inhibition of DNA methylation, but we cannot exclude the existence of indirect mechanisms operating on longer time scales. Our results confirmed that H2A.Z fosters H3K4me3 deposition but has a predominantly repressive impact on transcription, in line with broadening the barrier to elongating RNA Pol II [91], causing enhanced pausing and slowing down pre-initiation complex reloading [20]. Our approach uniquely allowed us to determine H2A.Z-independent functions of SRCAP. We found that SRCAP stimulates the transcription of house-keeping genes, in line with H2A.Z-independent upregulation of housekeeping genes by the Drosophila SRCAP-ortholog DOMINO during zygotic genome activation [1]. SRCAP also restricts genome-wide binding of a large number of TFs by blocking access to their binding sites. We propose steric hindrance as a new mechanism by which bulky DNA-binding complexes can restrict the access of TFs to chromatin.

The dynamic interplay between SRCAP and H2A.Z provides an elegant strategy to maintain cell identity of PSCs by robust, yet rapidly reversible restriction of both the expression and DNA-binding of lineage-specific TFs. The high degree of evolutionary conservation and the role of SRCAP/H2A.Z in self-renewal of multiple types of stem cells [5–7] suggests their broad involvement in the regulation of stem cell plasticity. We thus propose SRCAP/H2A.Z as a pivotal gene regulatory system operating in parallel to other epigenetic mechanisms to maintain cell identity and plasticity.

Acknowledgments

We thank the Gene Expression, Flow Cytometry, BioImaging and Biomolecular Screening core facilities at EPFL. We thank Dr Matthias Mann for kindly providing access to MS instrumentation, and to Dr Igor Paron and Dr Tim Heymann for outstanding MS technical assistance. We thank Dr Martin Pacesa for help in designing cdSRCAP. We thank Dr Ludovica Vanzan, Dr Nadine Vastenhouw and Dr Nicolas Thomä for their input. We are thankful for funding by the Swiss National Science Foundation grant#310030_184782 and# 310030_212197 to DMS. HL and EU are funded by the Deutsche Forschungsgemeinschaft (DFG, German Research Foundation, 213249687 - SFB1064 to H.L. (A17)). EU gratefully acknowledges the International Max Planck Research School for Molecular Life Sciences (IMPRS-LS) and the Research Training Group 1721 (RTG 1721) for training and support. The

work from SDL, DA and JCMG was funded by the Deutsche Forschungsgemeinschaft (DFG, German Research Foundation no. 468578170 and CRC 1506 C05 no. 450627322 to JCMG).

Authors Contributions

Conceptualization, AT and DMS; Methodology, AT, EU, SDL and DMS; Formal Analysis, AT, EU, SDL and DMS; Investigation, AT, EU, SDL and CD; Instrumentation (single molecule imaging microscope), DA; Resources, DMS, HL and JCMG; Writing Original manuscript, AT and DMS; Funding Acquisition, DMS, HL and JCMG; Supervision, DMS, HL and JCMG.

Competing interests

The authors declare no competing interests.

Data availability

All sequencing data were deposited at NCBI Gene Expression Omnibus (GEO), accession number GSE269310 (with token grkzuqcwplmnlkr).
Proteomics data were deposited at ProteomeXchange, accession number PXD052934 (with token bwU5076lLymG).

Extended data

Figures S1 to S7
Table S4: List of primers used in the study
Table S5: List of pioneer transcription factors

Supplementary Information

Table S1: Excel file containing RNA-Seq raw counts and differential analysis results
Table S2: Excel file containing results from proteome and chromatome analysis
Table S3: Excel file containing results from TF footprinting analysis

Methods

Resource Table

REAGENT or RESOURCE	SOURCE	IDENTIFIER
Antibodies		
Rabbit anti-H2A.Z	Abcam #ab4174	RRID:AB_304345
Acetyl-histone H2A.Z (K4,K7,K11)	ThermoFisher Scientific #PA540095	RRID:AB_2609565
Rabbit anti-H2A	Abcam #ab18255	RRID:AB_470265
Rabbit anti-GFP	Abcam #ab290	RRID:AB_2313768
Rabbit anti histone H3K4me3	Abcam #ab8580	RRID:AB_306649
Rabbit anti histone H3K27me3	Abcam #ab195477	RRID:AB_2819023
Rabbit anti histone H2AK119ub1	Cell Signaling Technology #8240	RRID:AB_10891618
Rabbit anti-YY1	Cell Signaling Technology #46395	RRID:AB_2799302
Mouse anti NF-Ya	Santa-Cruz Biotechnology #sc-17753	RRID:AB_628018
Rabbit anti-Oct4	Cell Signaling Technology #5677	N/A
Rabbit anti-Sox2	Cell Signaling Technology #23064	RRID:AB_2714146
Rabbit anti-Nanog	Cell Signaling Technology #8822	RRID:AB_11217637
Rabbit anti-SRCAP	Kerafast #ESL103	RRID:AB_3086743
Biological samples		
Chemicals, peptides, and recombinant proteins		
Indole-3-Acetic Acid (IAA)	Sigma-Aldrich #I5148	CAS: 6505-45-9
Auxinole	MedChemExpress #HY-111444	CAS:86445-22-9
GSK-3484862	MedChemExpress #HY-135146	CAS: 2170136-65-7
Deposited data		
GSE64825	De Dieuleveult et al. 2016 [92]	N/A
GSE48519	Hon et al. 2014 [93]	N/A
GSE143737	Mylonas et al. 2021[20]	N/A
Experimental models: Cell lines		
CGR8 (ESC Mus musculus)	Sigma-Aldrich #07032901	N/A
SYA (ESC Mus musculus)	This study	N/A
SYAT (ESC Mus musculus)	This study	N/A
SYAT-wtSRCAP (ESC Mus musculus)	This study	N/A
SYAT-cdSRCAP (ESC Mus musculus)	This study	N/A
ZHBTc4 (ESC Mus musculus)	Niwa et al., 2000 [34]	RRID: CVCL_C715
HEK-293T	ATCC	RRID:CVCL_0063
Oligonucleotides : List provided in Table S4		
Recombinant DNA		

psPAX2	Addgene	RRID: Addgene_12260
pMD2.G	Addgene	RRID: Addgene_12259
pX330	Addgene	RRID:Addgene_42230
pMK-Ypet-AID-P2A-Hygro	This study	N/A
pLV-EF1a-OsTir1-SNAP-P2A-Puro	This study	N/A
pLV-PGK-Ypet-MD	Deluz et al. 2016 [94]	N/A
pLV-PGK-mCherry-MD	This study	N/A
pLV-rtTA3G-Bsd	Deluz et al. 2016 [94]	N/A
pLV-TRE3G-wtSRCAP-mCherry	This study	N/A
pLV-TRE3G-cdSRCAP-mCherry	This study	N/A
pLV-TRE3G-Halo-Nanog	This study	N/A
pLV-pGK-Halo-Nanog	This study	N/A
Software and algorithms		
FiJi Version 2.14.0/1.54f	Schindelin et al., 2012 [95]	RRID:SCR_002285
STAR Version 2.7.6a	Dobin et al., 2013 [96]	RRID:SCR_015899
Picard Version 2.23.7	Broad Institute	RRID:SCR_006525
MACS Version 3.0.0a7	Zhang et al., 2008 [97]	RRID:SCR_013291
DeepTools Version 3.5.1	Ramírez et al., 2016 [98]	RRID:SCR_016366
Bedops Version 2.4.41	Neph et al., 2012 [99]	RRID:SCR_012865
BEDtools Version 2.30.0	Quinlan and Hall, 2010 [100]	RRID:SCR_006646
SAMtools Version 1.14	Li et al., 2009 [101]	RRID:SCR_002105
DANPOS2 Version 3.1.1	Chen et al. 2013 [102]	RRID:SCR_015527
Bwa-Meth	Pedersen et al. 2014 [103]	RRID:SCR_010910
MethylDackel Version 0.5.3	https://github.com/dpryan79/MethylDackel	
MethylKit Version 1.28.0	Akalin et al. 2012 [104]	RRID:SCR_005177
DeSeq2 Version 1.42.1	Love M.I et al. 2014 [105]	RRID:SCR_015687
edgeR Version 4.0.11	Robinson et al., 2010 [106]	RRID:SCR_012802
limma Version 3.58.1	Ritchie et al., 2015 [107]	RRID:SCR_010943
R studio Version 2023.12.0+369		RRID:SCR_000432
Cluster Profiler Version 4.10.1	Yu et al. 2012 [108]	RRID:SCR_016884
ggplot2 Version 3.5.0	Wickham, 2009 [109]	RRID:SCR_014601
ggrepel Version 0.9.5	Slowikowski K, 2024	
biomaRt Version 2.58.2	Durinck et al., 2005 [110]	RRID:SCR_002987
TOBIAS Version 0.13.3	Bentsen et al.,2020 [55]	
SEA Version 5.5.5	Bailey and Grant, 2021 [111]	RRID:SCR_001783
FreeSASA Version 2.1.2	Mitternacht, 2016 [112]	

Cell culture

CGR8 mouse ES cells (Sigma, Cat#07032901-1VL) and ZHBTc4 mouse ES cells[34] were routinely cultured at 37 °C and 5% CO_2 on cell culture-treated dishes coated with 0.1% gelatin

(Sigma #G9391-100G) using the following culture medium: GMEM (Sigma #G5154-500ML) supplemented with 10% ES cell-qualified fetal bovine serum (Gibco #16141–079), 1% nonessential amino acids (Gibco #11140–050), 2 mM L-glutamine (Gibco #25030–024), 2 mM sodium pyruvate (Sigma #S8636-100ML), 100 µM 2-mercaptoethanol (Sigma #63689–25 ML-F), 1% penicillin and streptomycin (BioConcept #4–01 F00-H), in-house produced leukemia inhibitory factor (LIF), CHIR99021 (Merck #361559–5 MG) at 3 µM and PD184352 (Sigma #PZ0181-25MG) at 0.8 µM. Cells were passaged by trypsinization (Sigma #T4049-100ML) every two to three days. Before all experiments, mESC medium was changed to Serum LIF medium: GMEM (Sigma #G5154-500ML) supplemented with 10% ES cell-qualified fetal bovine serum (Gibco #16141–079), nonessential amino acids (Gibco #11140–050), 2 mM L-glutamine (Gibco #25030–024), sodium pyruvate (Sigma #S8636-100ML), 100 µM 2-mercaptoethanol (Sigma #63689–25 ML-F), penicillin and streptomycin (BioConcept #4–01 F00-H), in-house produced leukemia inhibitory factor (LIF). SYAT cells were cultured routinely with 200 µM Auxinole (MedChemExpress #HY-111444) (Control condition) to avoid basal degradation of SRCAP. For SRCAP degradation, SYAT cells were treated for 1, 2, 4, 6 or 8 h with 500 µM Indole-3-Acetic Acid (IAA, Sigma-Aldrich #I5148). For induction of Oct4 knockdown in ZHBTc4 cells, 1 µg/mL Doxycycline was added for 9 or 12 h prior cell collection. For DNMT1 inhibition, SYAT cells were treated with 2 µM GSK-3484862 (MedChemExpress #HY-135146) for 5 days before performing ATAC-seq. All used cell lines were tested every 6 months for the absence of Mycoplasma by Eurofins Genomics.
For imaging, cells were plated on Laminin (1/10 dilution of Biolaminin (BioLamina, LN511-0202) in PBS). Prior imaging, medium was replaced by FluoroBrite DMEM (ThermoFisher, #A18967–01) supplemented with 10% ES cell-qualified fetal bovine serum (ThermoFisher, #16141079), 2 mM sodium pyruvate (Sigma-Aldrich, #113–24–6), 1% non-essential amino acids (ThermoFisher, #11140035), 1% penicillin/streptomycin (BioConcept, #4–01F00H), 2 mM L-glutamine (ThermoFisher, #25030–024), 100 µM 2-mercaptoethanol (Sigma-Aldrich, #63689–25ML-F) and LIF.

Lentiviral vector production

Lentiviral vectors were produced by transfection of HEK 293T cells with the envelope (psPAX2, Addgene #12260), packaging (pMD2.G, Addgene #12259) [113], and lentiviral construct of interest using Calcium Phosphate transfection, as described previously [114]. Viral vectors were concentrated 120-fold by ultracentrifugation at 20000 x *g* for 120 min at 4°C. 50000 cells in 500 µL of medium in a 24-well plate were transduced with 50 µl of concentrated lentiviral vector particles to generate stable cell lines.

Generation of SYA and SYAT cell lines

The SYA cell line was generated using CRISPR/Cas9-mediated homology-directed repair (HDR). A SRCAP gRNA designed using CRISPOR [115] to target the C-terminal part of mouse SRCAP was added in pX330-gRNA vector (pX330-gRNA was a gift from Charles P. Lai (Addgene plasmid #158973)) by digestion with BbsI to build pX330_SRCAP. The Ypet_AID_P2A_Hygromycin-resistance cassette was amplified with primers containing 60bp homology arms corresponding to the carboxy-terminal part of SRCAP and 2µg of amplicons were co-transfected in $1.5x10^6$ CGR8 mouse ES cells together with 2 µg of pX330-SRCAP using Lipofectamine 3000 (ThermoFisher Scientific #L3000008). Cells were selected by addition of 150 µg/mL Hygromycin 72 h post-transfection for a week before individual clones were picked. gDNA was extracted using Direct PCR Lysis (Viagen Biotech, #301-C) and incubated 2 h at 55°C, 30 min at 85°C followed by 5 min at 95°C. Clones were characterized by PCR using primers annealing to the SRCAP locus and in the knock-in cassette (Table S4), followed by visualization of the Ypet signal intensity and nuclear localization by live imaging using the YFP channel on a IN Cell Analyzer 2200 apparatus (GE healthcare). One homozygous clone of SYA cells was then transduced with a lentiviral vector containing EF1a-OsTir1-SNAP-P2A-puro and selected with 2 µg/ml of Puromycin (Gibco A11138-03) for a week. To select for cells efficiently degrading SRCAP upon IAA treatment, SYAT cells were treated for 2 h with IAA prior sorting for Ypet-negative cells.

SRCAP constructs and cell line generation

SRCAP was amplified from cDNA of CGR8 cells in 3 separate PCR fragments. To generate the catalytically-dead mutant, mutations were introduced in the Rev primer of the first fragment and the Fw primer of the second fragment (see Table S4 for primer sequences). The three fragments and the pLV-TRE3G-mCherry cut with SalI upstream of the mCherry coding sequence were assembled using In-fusion cloning (Takara Bio # 638947) and the obtained products were transformed into home-made HB101 competent bacteria. Clones were then screened by PCR for the presence of full length SRCAP and sequenced to verify the presence of the mutated sequence. Correct clones were used to produce lentiviral particles to transduce SYAT cells together with a lentiviral vector expressing rtTA3G and a blasticidin resistance. After selection with 5 µg/mL blasticidin for a week, cells were treated with 1µg/mL of dox for 24 h to induce expression of SRCAP-mCherry, prior to cell sorting for mCherry-positive cells and isolation of single cells. One clone for wtSRCAP and one clone for cdSRCAP were selected by FACS for similar mCherry levels. Prior to all experiments, wtSRCAP and cdSRCAP were induced with 1 µg/mL Doxycyline for 24 h, treated with 500 µM IAA for 4 h or left in 200 µM Auxinole (Control) and sorted for similar and high mCherry expression just before performing ChIP-Seq, ATAC-Seq or nuclear RNA-Seq.

FACS for different cell cycle phases

For mitotic ChIP, $12x10^6$ cells were collected by mitotic shake-off, fixed 10 min with 1% formaldehyde (ThermoFisher #28908) at room temperature (RT) prior to quenching with 250 mM Tris-HCl pH8. Next, staining with 50 mM Hoechst33342 (Thermo Fisher Scientific #H3570) was performed for 15 min at RT. Cells were then permeabilized by addition of ice-cold 70% ethanol and stained with an anti-H3S10P antibody (Merck-Millipore, 05-1336) diluted 1:1000 for 1 h at 4°C. Samples were stained with Alexa-Fluor 647 anti-rabbit (H+L) secondary antibody (ThermoFisher Scientific #A-31571) for 45 min at 4°C. Mitotic cells were selected by FACS as Hoechst-high and H3S10P-positive. For other cell cycle phases, we used CGR8 cells stably expressing Ypet fused to a mitotic degron (MD) or SYAT cells stably expressing mCherry-MD stained with Hoechst, followed by sorting according to Hoechst and Ypet/mCherry intensities: Hoechst-low/Ypet-low/mCherry-low cells being in early G1 phase, Hoechst-low/Ypet-high/mCherry-high in late G1 phase, intermediate-Hoechst in S phase and Hoechst-high in G2M phase. For sorting cells at the end of mitosis, SYAT cells expressing mCherry-MD and stained with Hoechst were selected for Hoechst-high/mCherry-low intensities. All FACS were performed on a FACSAria II or a FACSAria Fusion (BD Biosciences).

Immunofluorescence

SYAT or wt CGR8 cells were plated on 1:10 diluted Biolaminin (BioLamina, LN511-0202) in DPBS (Gibco, 14040091) in 96-well plates with black walls or 3.5 mm dishes. Cells were fixed with 2% Formaldehyde diluted in DPBS for 30 min at RT. Permeabilization was then performed by addition of a solution of 0.5% Triton X-100 (AppliChem, A1388,0500) for 30 min before addition of blocking solution (BSA 1% (Sigma-Aldrich, A7906) in DPBS) for 30 min. An anti-H2A.Z antibody (Abcam ab4174) was diluted 1:1000 in blocking solution prior to incubation overnight at 4°C, followed by three washes with 0.1% Tween-20 diluted in DPBS. The secondary antibody Alexa-Fluor-647 Chicken anti-rabbit IgG (H+L) (ThermoFisher Scientific #A-21443), was diluted 1:1000 in blocking buffer and incubated for 1 h at RT. Cells were then washed three times with 0.1% Tween-20 diluted in DPBS and twice with DPBS before addition of DAPI-Fluoromount G (SouthernBiotech, #0100-20). Imaging was performed on an IN Cell Analyzer 2200 apparatus (GE healthcare) using a 20X magnification objective and the YFP fluorescence channel for Ypet detection, the Cy5 fluorescence channel for AF-647 detection and DAPI fluorescence channel for DAPI detection. For high magnification imaging of mitotic chromosomes, imaging was performed on a spinning disk microscope (Visitron CSU-W1) with a 60X objective. For image quantification, the Fiji software[95] was used to subtract background and manually determine the area of the region of interest (ROI) and the intensities for the different channels. For each channel, integrated intensities were calculated by multiplying the

mean fluorescence intensity by the area of the ROI. Around 50 cells were quantified for each treatment condition and phase.

Pluripotency assay and RT-qPCR

600 SYAT or CGR8 cells were plated in 6-well plates and cultured in GMEM-Serum-2i-LIF for 5 days. Cells were stained with Phosphatase Alkaline staining kit (Merck-Millipore, SCR004) according to the manufacturer instructions.

For RT-qPCR experiments, RNA was extracted from $3x10^6$ SYAT or CGR8 cells with the Rneasy Plus Mini Kit (Qiagen, #74134). Reverse transcription was performed on 1 µg RNA using oligodT (Thermo Fisher Scientific #SO131) and Maxima H minus First Strand cDNA synthesis (Thermo Fisher Scientific #K1652). The RT reaction was diluted 1/10 prior to qPCR. Primers used to amplify *Rps5*, *Zfp42*, *Pou5f1*, *Sox2*, *Nanog*, *Esrrb* and *c-Myc* are detailed in Table S4. Plates were assembled using an automated Hamilton liquid handling platform and analyzed on a QuantStudio 7 (Applied Biosystem). Relative quantifications were obtained by normalization on *Rps5* mRNA levels.

ChIP-Seq

For histones and histone post-translational modifications, cells were fixed for 10 min with 1% formaldehyde at RT. For transcription factors, cells were fixed with 2 mM disuccinimidyl glutarate (Thermo Fisher Scientific #20593) for 50 min and in 1% formaldehyde for 10 min. In both cases, fixation was quenched with 250 mM Tris-HCl pH8. All fixed cell pellets except mitotic samples were kept on ice and resuspended in Lysis Buffer 1 (50 mM HEPES-KOH pH 7.4, 140 mM NaCl, 1 mM EDTA, 0.5 mM EGTA, 10% Glycerol, 0.5% NP-40, 0.25% Triton X-100 supplemented with Protease inhibitor cocktail (Sigma #P8340-1ML) at 1:100 dilution), incubated 10 min at 4°C, spun down at 1700 x *g*, and resuspended in LB1 a second time, spun down and resuspended in Lysis Buffer 2 (10 mM Tris-HCl pH 8.0, 200 mM NaCl, 1 mM EDTA, 0.5 mM EGTA supplemented with Protease inhibitor cocktail (Sigma #P8340-1ML) at 1:100 dilution), incubated for 10 min at 4°C, spun down and washed without disturbing the pellet twice with SDS shearing buffer (10 mM Tris-HCl pH 8.0, 1 mM EDTA, 0.15% SDS supplemented with Protease inhibitor cocktail (Sigma #P8340-1ML) at 1:100 dilution)) and finally resuspended in SDS shearing buffer. For mitotic samples, cell pellets were washed twice in SDS shearing buffer and then resuspended in SDS Shearing buffer. Chromatin was sonicated for 20 min at 5% duty cycle, 140 W, 200 cycles or for sorted samples for 10 min at 10% duty, 75W, 200 cycles on a Covaris E220 focused ultrasonicator. ChIPs were then performed using ChIP-IT High Sensitivity kit (Active motif, #53040), following manufacturer instructions. 10 ng of Drosophila spike-in chromatin (Active motif, 53083) and 0.5µg of spike-in antibody (anti-H2Av, Active motif, 61686) were processed together with mouse ES cell

chromatin (1.5 µg for ChIP-seq on mitotic cells and matching asynchronous cells, 4 µg for the other H2A.Z and H2A ChIP-seq, 2 µg for H3K4me3, H3K27me3 and H2AK119ub1 and 5 µg for ChIP-seq against TFs) as an internal experiment calibrator [116]. Libraries were prepared with the NEBNext Ultra II DNA Library Prep Kit (NEB #E7645) and sequenced on an Illumina NextSeq 500 using 75-nucleotide read length paired-end sequencing.

CUT&Tag

CUT&Tag experiments were performed in duplicates using the CUT&Tag-IT Assay Kit (Active Motif #53160) and following manufacturer instructions. Briefly, 200,000 SYAT cells were bound on Concanavalin A beads prior to incubation overnight with 1:50 anti-GFP rabbit antibody (Abcam #ab290). Next, cells were incubated with a secondary antibody, pA-Tn5-transposomes, and washed according to manufacturer instructions. Transposition was subsequently performed for 1 h at 37°C, and transposed DNA was purified prior to Library Preparation and size exclusion with SPRI beads using a 0.5X ratio while keeping the unbound fraction and 1X ratio on the left side, taking the bound fraction. Libraries were sequenced on an Illumina NextSeq 500 using 75 nucleotide read-length paired-end sequencing.

CUT&RUN

CUT&RUN was performed on 100,000 SYAT cells using an anti-SRCAP antibody (Kerafast #ESL103) following the protocol used in [117].

ATAC-Seq

All ATAC-seq experiments were performed in biological duplicates. 50,000 cells were collected either directly after trypsinization or after sorting as described above, and subjected to ATAC-seq as described previously[118]. All centrifugation steps were done at 800 x *g* at 4°C. Briefly, cells were centrifuged for 5 min and washed with cold PBS, then centrifuged for 5 min and resuspended in cold lysis buffer (10 mM Tris-HCl pH 7.4, 10 mM NaCl, 3 mM MgCl2, 0.1% NP-40), and centrifuged for 10 min. Subsequently, nuclei were resuspended in a solution of 0.5 mM Tn5 (in-house preparation according to [119]) in TAPS-DMF buffer (10 mM TAPS-NaOH, 5 mM Mgcl2, 10% DMF) and incubated for 30 min at 37°C. DNA was immediately purified using column purification (Zymo #D4004) and eluted in 10 µl nuclease-free water. Transposed DNA was amplified in a solution containing 1X NEBNextHigh Fidelity PCR Master Mix (NEB #M0541L), 0.5 µM of Ad1.1 universal primer, 0.5 µM of Ad2.x indexing primer and 0.6x SYBR Green I (Thermo Fisher Scientific #S7585) using 72°C for 5 min, 98°C for 30 s, and 5 cycles of 98°C for 1 s, 63°C for 30 s, and 72°C for 60 s. 10 µl of amplified DNA was analyzed by qPCR to determine the total number of cycles to avoid amplification saturation and accordingly amplified with additional 3–7 cycles at 98°C for 10 s, 63°C for 30 s, and 72°C for 60 s. DNA

was purified using column purification (Zymo #D4004) and size-selected by taking the unbound fraction of 0.55X AMPure XP beads (Beckman Coulter #A63880) followed by the bound fraction of 1.2X AMPure XP beads. Libraries were sequenced on an Illumina NextSeq 500 using 75 nucleotide read-length paired-end sequencing.

Nuclear RNA-Seq

All RNA-Seq experiments were performed in biological duplicates. Following cell collection and wash in PBS, cell pellets were resuspended in 500 µL Nuclear RNA lysis buffer (10 mM Tris pH 7.4, 10 mM NaCl, 3 mM MgCl2, 1% BSA (Merck, #B9000S), 0.1% Tween (Fisher Scientific, #10113103), 1 mM DTT (Merck, #646563), 0.5 U/µl Protector RNase Inhibitor (Merck, #3335399001), 0.1% NP-40, 0.01% Digitonin (Invitrogen, #BN2006)) and incubated 5 min on ice. Then 500 µL Nuclear RNA wash buffer (10 mM Tris pH 7.4, 10 mM NaCl, 3 mM MgCl2, 1% BSA (Merck, #B9000S), 0.1% Tween (Fisher Scientific, #10113103), 1 mM DTT (Merck, #646563), 0.5 U/µl Protector RNase Inhibitor (Merck, #3335402001) were added before spinning down cells at 300 x *g* 4°C for 5 min. Two more washes with Nuclear RNA wash buffer were performed before proceeding to RNA extraction using the Rneasy Plus Micro Kit (Qiagen, #74034) with the addition of an on-column DNAse digestion (Qiagen, #79254). Sequencing libraries were prepared by the EPFL Gene Expression Core Facility using the NEBNext Ultra II Directional RNA Library Prep Kit for Illumina (NEB, #E7760S), and sequenced on a NovaSeq6000 using 75-nucleotide read length paired-end sequencing.

MNAse-Seq

All MNAse-Seq experiments were performed in triplicates according to the following protocol[120]. Briefly, Micrococcal Nuclease S7 (Roche #10107921001) was resuspended to 15 U/µL in 20 mM Tris-HCl pH 7.5, 50 mM NaCl, 50% Glycerol. For high digestion condition, MNase was diluted at 100 U/mL in MNase Digestion buffer (50 mM Tris-HCl pH 8, 150 mM sucrose, 50 mM NaCl, 5 mM $CaCl_2$). For low digestion condition, MNase was diluted at 6.25 U/mL in MNase Digestion Buffer. SYAT cells were treated for 4 h with 500 µM IAA or 200 µM Auxinole before collection. $5x10^6$ cells were used for each MNase digestion condition. After cell collection, cell pellets were resuspended in 50 µL Resuspension Buffer (35 mM HEPES pH 7.4, 150 mM sucrose, 80 mM KCl, 5 mM KH_2PO_4, 5 mM $MgCl_2$, 0.2% NP-40). Then, 500 µL of MNase solution were added to the cells and incubated for exactly 10 min at 37°C before inactivation of MNase by addition of 11 µL of 0.5 M EDTA to the reaction. Next, 550 µL of Lysis Buffer (50 mM Tris-HCl pH 8, 1% SDS, 10 mM EDTA) was added and samples were incubated on ice for 10 min. After addition of 1.1 mL DNAse-free water, samples were digested for 2 h at 37°C with RNase (50 µg per reaction). Finally, 3200 U of Proteinase K were added, and digestion was performed at 56°C for 2 h. Digested DNA was purified using a DNA Purification

kit (Active Motif #58002). Then, 500 ng of DNA for the High digestion condition and 1500 ng of DNA for the Low digestion condition were loaded on a 1.5% agarose gel and the band below 200bp was cut out and gel-purified. Library preparation was carried out on the purified DNA using NEBNext Ultra II DNA Library Prep Kit (NEB #E7645) and sequenced at 100 million reads per sample on a NovaSeq6000 using 75-nucleotide read length paired-end sequencing.

Enzymatic Methyl-Sequencing

EM-Seq experiments were performed in duplicate. Genomic DNA was extracted using a DNeasy Blood and Tissue kit (Qiagen #69504) and repurified using a DNA Clean and Concentrator-5 Kit (Zymo #D4004). Next, 200 ng of purified genomic DNA were sonicated for 90 s, 10% duty, 140 W, 200 cycles on a Covaris E220 focused ultrasonicator and were subsequently processed using NEBNext Enzymatic Methyl-Seq kit (NEB #7120) following the manufacturer protocol. Libraries were sequenced at 200 million reads per sample on a NovaSeq6000 using 75-nucleotide read length paired-end sequencing.

Whole Proteome and chromatome analysis by Mass Spectrometry

The whole proteome and chromatome sample preparation, liquid chromatography followed by tandem mass spectrometry (LC-MS/MS) and data analysis were performed as previously described in [58], with a few adjustments: for the whole proteome-chromatome-matched sample collection, 7 x 10^6 embryonic stem cells were harvested per condition and replicate. The cells were washed with PBS and split into two parts: 2 x 10^6 cells for whole proteome analysis and 5 x 10^6 cells for chromatome analysis. Liquid chromatography was performed using the EvosepONE system with a 15 cm × 150 µm column containing 1.9 µm C18 beads (PepSep). Each sample (200 ng) was loaded onto Evotips according to the manufacturer's protocol. The gradient length was 44 minutes (30SPD). The column temperature was maintained at 40°C, and electrospray ionization was achieved using a stainless-steel emitter (30 µm inner diameter) at 2.2 kV. Mass spectrometry was conducted on an Orbitrap Exploris™ 480 mass spectrometer (Thermo Fisher Scientific) in data-independent acquisition (DIA) mode. MS1 acquisitions were performed as previously described, using an orbitrap resolution of 120,000 with a scan range of 350-1400 m/z and a maximum injection time of 45 ms. For the MS2 acquisition, adjustments were made to accommodate the shorter LC gradient. Specifically, 49 scan events were performed with isolation windows of 13.7 m/z at an orbitrap resolution of 15,000. The normalized AGC target was set to 3000%, and the maximum injection time was 22 ms. The precursor mass range was maintained at 361-1033 m/z.

The list of TF was determined using a list of proteins associated with the GO terms DNA-binding transcription factor activity (GO:0003700) and Sequence-specific DNA binding (GO:0043565).

Single-molecule imaging

We performed single-molecule imaging on SYAT, wtSRCAP and cdSRCAP cells over-expressing Halo-Nanog under the control of doxycycline-inducible TRE3G or constitutive pGK promoters, respectively. We seeded cells on 35 mm glass bottom dishes (Ibidi, 81158) previously coated with a 1:10 dilution of Biolaminin in PBS. 72 h prior imaging, we added 200 µM Auxinole to the culture medium for all cell lines. For SYAT cells, we induced expression of Halo-Nanog by adding 0.5 µg/ml Doxycycline, 24h before imaging. Staining was performed right before Doxycycline induction, 24-25h prior to imaging. We stained SYAT cells for single-molecule tracking with 100 pM or 25 pM HTL-SiR (kindly gifted by Kai Johnsson, MPI Heidelberg), respectively, for 85 Hz or 0.5 Hz movies. To visualize the nucleus, we performed additional staining with 62 nM HTL-TMR (Promega, G8252). After staining, cells were incubated for 30 minutes, then washed twice with PBS and incubated overnight in medium containing 0.5 µg/ml Doxycycline. To induce SRCAP degradation, we washed cells twice with PBS to remove residual auxinole and treated SYAT cells with 500 µM IAA 4h before imaging. Cells were then washed three times with PBS and imaged in OptiMEM. We induced the expression wtSRCAP and cdSRCAP cells by adding 1 µg/ml Doxycycline 24 h before imaging. cdSRCAP cells were stained with 1 pM or 5 pM HTL-SiR, respectively, for 85 Hz or 0.5 Hz movies. wtSRCAP cells were stained with 50 pM HTL-SiR for both types of movies. The incubation time was in all cases 15 minutes. We subsequently washed cells three times with PBS and imaged in OptiMEM.

Single-molecule tracking experiments were conducted on a custom-built inverted microscope with highly inclined laminated optical sheet (HILO) illumination [121]. The fluorophores were excited with a 638 nm laser (Omicron Luxx Laser, Omicron-Laserage Laserprodukte Gmbh), which was spatially cleaned by a single mode fiber (kineFLEX HPV, Excelitas Technologies Corp.). The beam was further expanded to a FWHM diameter of around 6mm with a fiber-coupler (60FC-T-4-M50L-0, Schäfter+Kirchhoff GmbH) and its profile was altered from a gaussian to a flattop via a diffractive beam shaper (piShaper 6_6_VIS, AdlOprica GmbH). The laser was focused into the back-focal plane of the objective (CFI SR HP Apochromat TIRF 100xC Öl, Nikon GmbH) over an achromatic lens (AC254-200-A, Thorlabs GmbH) and a dichroic mirror (F73-537, AHF Analysetechnik). The fluorescence light was filtered by a combination of an emission and a notch filter (F67-532 and F40-074, AHF Analysetechnik) and detected on a sCMOS camera (Prime BSI, Teledyne Scientific Imaging GmbH). Pixels on the sCMOS camera were binned 2x2 resulting in an effective pixel size of 130nm. The sample

was mounted in a stage incubator (Inkubator XS 2000, PeCon GmbH) with 37°C and 5 % CO2 and was controlled in x-y-z direction with two stacked piezo stages (M-686 and M-562, Physik Instrumente GmbH).

To determine the diffusion coefficients and bound fraction of Halo-NANOG, we performed tracking of molecules with a camera exposure time of 10 ms. Each cell was imaged only once. SYAT cells were imaged with a 638 nm laser at 650 µW for 2500 consecutive frames. cdSRCAP and wtSRCAP cells were selected for low or zero Ypet signal, and additionally for high mCherry signal in the case of + dox measurements, then imaged with a 638 nm laser at 780 µW for 2000 consecutive frames.

To determine the chromatin residence time of Halo-NANOG, we performed measurements with a camera exposure time of 500 ms at continuous illumination (continuous illumination) or alternating between a single illuminated frame and a fixed dark time of 10 s (time-lapse illumination). For both illumination schemes and for all the cell lines, we imaged with a 638 nm laser at 30 µW. Each cell was only imaged once. Global analysis of both illumination schemes allowed us to differentiate between dissociation of molecules and photobleaching or tracking errors, respectively [79].

Analysis of single-molecule movies

Analysis of single-molecule tracking data was performed using TrackIt [78]. For 85 Hz movies, spots were detected with a threshold factor of 1 and a tracking radius of 4 px. For 0.5 Hz movies, we selected threshold factors of 1.0, 1.4 and 1.3, respectively for the SYAT, the wtSRCAP and the cdSRCAP cell line. The tracking radii were 3 px for the continuous and 5 px for the time-lapse illumination, for all cell lines. The minimum tracking length was 2 frames for all conditions and cell lines, allowing for one gap frame if the track lasted longer than 2 frames. We determined diffusion coefficients and fractions for Halo-NANOG by fitting the cumulative distribution of squared jump distances obtained from the 85 Hz movies with a 3-component diffusion model [77]. To estimate the error for every diffusion coefficient we repeated the analysis 400 times, with 80% of randomly selected jump distances. The overall bound fraction of Halo-NANOG was defined as the amplitude A1 of the slowest apparent diffusion component, originating from the localization error and slow chromatin movement. The other two components A2 and A3 accounted for anomalous diffusion in the nucleus [122,123]. Next, we determined the dissociation rates of Halo-NANOG from chromatin using GRID [79]. GRID generates a spectrum of dissociation rates by inverse Laplace transformation of the distribution of fluorescence survival times for Halo-NANOG-bound SiR. An estimate of the error associated to each dissociation rate was given by repeating GRID analysis 500 times with 80% of randomly selected data from the survival time distributions. The residence times of Halo-NANOG were calculated as the inverse of the dissociation rates. For further analysis, we

focused on the longest residence times, as this is typically associated with the specific function of a transcription factor [124–126]. The absolute fraction of long-bound molecules was calculated as the product of the overall bound fraction with the amplitude of the state spectrum associated with the longest binding time. The binding frequencies for Halo-NANOG were calculated as the inverse of the search times determined from bound fractions and dissociation rates as described [80,127].

ChIP-Seq and CUT&Tag analysis

Newly-generated ChIP-sequencing libraries, as well as ChIP-Seq for BRG1, Ep400, CHD4, H3K27ac, H3K4me1, H2A.Z.1 and H2A.Z.2 that were reanalyzed, were mapped to mm10 version of Mus musculus genome or version BDGP6 of Drosophila Melanogaster genome, using STAR [96] with parameters --alignMatesGapMax 2000 --alignIntronMax 1 --alignEndsType EndtoEnd --outFilterMultimapNmax 1. For NANOG ChIP performed on SYAT treated with different doses of IAA for 2 hours, raw sequencing files from two replicates were pooled prior mapping to the genome to increase sequencing depth. Duplicated reads and reads not mapping to chromosome 1-19 and X or Y were removed using Picard (Broad Institute). For the generated Drosophila alignments bam file, the number of reads was determined, and normalization factors were calculated to bring all the Drosophila bam files to the same number of reads. These normalization factors were then applied to downsample alignment files mapped on the mouse genome using SAMTools [101]. Peak calling was then performed on these downsampled bam files using MACS2 [97] with settings -f BAMPE -g mm, regions contained in mm10 blacklist from ENCODE consortium being excluded. Scores were determined from downsampled bam files using the bamCoverage function from DeepTools [98] with setting --normalizeUsing RPKM.

For score comparison, a bed file regrouping all peaks called in at least one condition was generated, and enrichment was calculated in these defined regions using the multiBigwigSummary function from DeepTools. For classification based on differences of peak amplitude between two time points of IAA treatment or with control, peaks were considered to be different in amplitude if there was a variation of at least 20% of enrichment score in peaks (RPKM-normalized) for H2A.Z, H3K4me3, H3K27me3 and H2AK119ub or at least 30% for YY1, NFYa, OCT4, SOX2, NANOG and H2A.Z in mitotic and asynchronous cells treated with IAA for 1 h or control.

For H2A.Z ChIP-Seq performed across the cell cycle, promoter and enhancer clusters were determined by k-mean clustering of the log2 fold-change of the signal between G2 and M phase together with log2 fold-change of the signal between M and EG1 phases, using the plotHeatmap function of DeepTools.

For H2A.Z ChIP in wtSRCAP or cdSRCAP-expressing SYAT cells, peaks were considered as rescued if the difference between IAA and Control enrichment scores was higher (with a 10% margin) in cdSRCAP compared to wtSRCAP.
In boxplots, the edges of the box represent respectively the first and third quartiles (Q1 and Q3), the bar represent the median value and the dots are the outlier values (lower than Q1-1.5xInterquartile-range, higher than Q3+1.5xInterquartile-range).

Establishment of reference bed files

The list of promoters was determined from a list of TSS in mm10 genomes (obtained from refTSS from the UCSC Genome Browser) that was enlarged from 1kb upstream the TSS and 500pb downstream. To determine the list of active promoters, this list was crossed with H3K4me3 peaks without any repressive histone marks, for bivalent promoters with peaks from H3K4me3 and H3K27me3 ChIP-Seq and for inactive promoters with H3K27me3 peaks that overlapped with no activating histone marks. To identify active enhancers, promoter regions were excluded and then H3K27ac peaks were crossed with H3K4me1 peaks. Poised enhancers were determined by crossing H3K4me1 enrichment with H3K27me3 enrichment. Regions outside promoters and without H3K4me1 enrichment were classified as inactive enhancers. For analysis using all enhancers grouped together, the list from the FANTOM5 consortium was used, or alternatively we used the list from Enhancer Atlas [128] established in J1 mESCs when promoter-enhancer loop information was required. To determine the number of promoter-enhancer loops, the number of enhancers interacting with one given gene was computed using the Enhancer Atlas list, separating upregulated genes from downregulated genes upon SRCAP depletion.
The list of TSS was enlarged from 20bp upstream and 20bp downstream of the TSS to determine the position of the TSS-nucleosome. Then the 400pb upstream of this position and 400pb downstream were considered as regions of positioning for the -1 or +1 nucleosomes, respectively.
Enhancer RNAs were defined as follows: the middle position of enhancers from the J1 enhancer list was determined and RNA reads falling into 3kb upstream and downstream were extracted, except those falling into exons and long non-coding RNA (list taken from LncRBase, http://bicresources.jcbose.ac.in/zhumur/lncrbase/).
H2A.Z.1-only, H2A.Z.2-only and shared peaks were determined by intersecting bed files generated from ChIP-Seq reanalysis of data from [20] using the bedtools intersect function. OCT4-dependent, SOX2-dependent, and co-dependent regions were extracted from a previous study [33].

MNAse-Seq analysis

MNAse-Seq libraries were mapped and filtered as described for ChIP-Seq. Nucleosome positions were determined using the dpos function from DANPOS2 [102]. Enrichment scores were computed using the bamCoverage function from DeepTools [98] with the setting --normalizeUsing RPKM. For all nucleosomes determined using DANPOS, the H2A.Z enrichment score was calculated, and nucleosomes were classified into "No H2A.Z" (3% lowest H2A.Z scores), "low H2A.Z" (1st quartile except "No H2A.Z"), "High H2A.Z" (Upper quartile) and "Intermediate H2A.Z" (remaining nucleosomes). These nucleosomes were further classified depending on whether they were in promoters or enhancers and according to the activity of these regulatory regions. Occupancy data were extracted from comparison of MNhigh and MNlow datasets using DANPOS. For MNase sensitivity, MNhigh and MNlow scores were determined for all nucleosomes using the multiBigwigSummary function from DeepTools and the MNlow over MNhigh ratio was calculated. For fragment length analysis, subsets of bam files were generated according to H2A.Z enrichment and regulatory regions using the samtools view function with parameters -b -h -L. The lengths of the fragments in the bam files were then determined with the samtools view -f66 | cut -f 9 command line.

Nuclear RNA-Seq analysis

Nuclear RNA-Seq libraries were mapped to the mm10 mouse genome using STAR. Exon coordinates were gathered from GENCODE annotation from vM25 of the UCSC Genome Browser. Introns coordinates were determined by subtracting exon coordinates from full length gene bodies using a script generated in a previous study (https://github.com/charitylaw/Intron-reads, [129]). Gene counts were then determined using the featureCounts function [130] from the R package Rsubread. Differential enrichment analysis as well as normalization of results using the lfcShrink function with type ="normal" were performed using DeSeq2 [105]. Reads counts were normalized on introns length and in transcript per million (TPM) for analysis of absolute RNA levels in control condition.

The bivalent genes list was determined from the list of bivalent promoters. The list of housekeeping genes was taken from a previous study [131]. Finally, the list of genes associated with pluripotency, mesoderm commitment, ectoderm commitment and endoderm commitment were compiled from Datanode using the terms "Mechanism associated with pluripotency (WP1763)", "Mesodermal commitment pathway (WP2857)", "Ectoderm differentiation (WP2858)" and "Endoderm differentiation (WP2853)", respectively.

For k-mean clustering of gene expression between wtSRCAP and cdSRCAP treated with IAA or control, intronic reads count for genes affected in at least one condition were normalized by DeSeq2 using the median of ratios method. Then for each gene, the z-scores across samples were computed. K-mean clustering was next performed using the pheatmap function from

pheatmap R package (https://CRAN.R-project.org/package=pheatmap) using a fixed number of 6 clusters.

EM-Seq analysis

Libraries were mapped using bwa-meth from Bwa (from Brent Pedersen, https://github.com/brentp/bwa-meth). CpG methylation was then calculated using MethylDackel (https://github.com/dpryan79/MethylDackel) before analysis of Differential methylation using MethylKit [104]. CpG methylation was computed for H2A.Z peaks located in promoters and enhancers and if the percentage of methylation was increased or decreased by 5%, regions were considered as hypermethylated or hypomethylated, respectively.

ATAC-Seq analysis

ATAC-Seq libraries were mapped and filtered as described for ChIP-Seq. The alignment files were subsequently downsampled so that all files contain the same total number of reads. Accessible peaks were then called, and scores were computed as described above for ChIP-Seq. Differentially-accessible regions were determined among peaks that had been called in at least one condition, for scores that varied from at least 30% between control and 4 h of IAA treatment.

TOBIAS analysis

For TOBIAS analysis, alignment files from ATAC-Seq were normalized with trimmed mean of M values (TMM) using calcNormfactors from edgeR with the TMM method followed by downsampling using SAMTools. Then, a correction of Tn5 bias was performed using TOBIAS ATACCorrect in all accessible regions in SYAT treated with control or IAA, excluding mm10 ENCODE-blacklisted regions. Footprints were then assessed with TOBIAS FootprintScore in the same regions. Finally, conditions were compared using TOBIAS BINDetect on the same regions or H2A.Z-rescued regions when specified, using the Jaspar2022 [132] non-redundant core list of motifs to which the Nanog motif (UN0383.1) was manually added.

The list of pioneer transcription factors (pTFs) (Table S5) was compiled from the list published by Lemma et al. [56] in their supplementary Table 4 and Peng et al. [57] in their supplementary Table 5 and 6.

For determination of motifs containing a CpG, power weight matrices (PWM) for all motifs were collected and the CpG score was calculated as follows.

For a motif with N positions :

$$CpG\ score = \sum_{i=1}^{N-1} P(C)_i \times P(G)_{i+1} \times (Weight_i + Weight_{i+1})$$

With for each position i,

$$P(C)_i = \frac{Score(C)_i}{Score(A)_i + Score(T)_i + Score(G)_i + Score(C)_i}$$

And

$$Weight_i = \frac{Score(A)_i + Score(T)_i + Score(G)_i + Score(C)_i}{mean(Score_{matrix})}$$

$mean(Score_{matrix})$ being the mean of all the scores present in the position weight matrix.
Then, motifs with a CpG score > 6 were considered as containing at least one CpG.
The P/E score was calculated for each motif as the likelihood that each motif occurrence is present in a promoter rather than an enhancer. For each occurrence of a motif present in a promoter the score is 1, if it is in an enhancer, it is 0. These scores are then averaged over all motif occurrences to give the P/E score of each TF motif.
For k-mean clustering of TF predicted binding scores in wtSRCAP and cdSRCAP treated with IAA or control, TF binding scores were extracted from TOBIAS results for all motifs of the Jaspar2022 database and the Nanog motif. Z-scores were then calculated across samples for each motif and k-mean-clustered using the pheatmap function with a fixed number of 6 clusters.

Motif and Gene Ontology (GO) enrichment

Motif enrichment was performed using the SEA algorithm [111] from the MEME suite using Jaspar non redundant core database as motif database and the default parameters for the other settings. GO enrichment analysis was performed using GOnet [133] with the default parameters and either biological process or molecular function filters for GO terms.

Published datasets

BRG1, Ep400, CHD4 ChIP-Seq raw datasets were obtained from GSE64825 [92]. H3K27ac, H3K4me1, H3K27me3 datasets were obtained from GSE48519 [93]. H2A.Z.1 and H2A.Z.2 ChIP raw datasets were obtained from GSE143737 [20].

References

1. Ibarra-Morales, D. *et al.* Histone variant H2A.Z regulates zygotic genome activation. *Nat Commun* **12**, 7002 (2021).
2. Hickey, G. J. *et al.* Establishment of developmental gene silencing by ordered polycomb complex recruitment in early zebrafish embryos. *eLife* **11**, e67738 (2022).
3. Liu, X. *et al.* Hierarchical Accumulation of Histone Variant H2A.Z Regulates Transcriptional States and Histone Modifications in Early Mammalian Embryos. *Advanced Science* **9**, 2200057 (2022).

4. Matsuda, R. *et al.* Identification and characterization of the two isoforms of the vertebrate H2A.Z histone variant. *Nucleic Acids Research* **38**, 4263–4273 (2010).
5. Hu, G. *et al.* H2A.Z Facilitates Access of Active and Repressive Complexes to Chromatin in Embryonic Stem Cell Self-Renewal and Differentiation. *Cell Stem Cell* **12**, 180–192 (2013).
6. Yu, H. *et al.* INO80 promotes H2A.Z occupancy to regulate cell fate transition in pluripotent stem cells. *Nucleic Acids Research* **49**, 6739–6755 (2021).
7. Zhao, B. *et al.* Znhit1 controls intestinal stem cell maintenance by regulating H2A.Z incorporation. *Nat Commun* **10**, 1071 (2019).
8. Wong, M. M., Cox, L. K. & Chrivia, J. C. The Chromatin Remodeling Protein, SRCAP, Is Critical for Deposition of the Histone Variant H2A.Z at Promoters *. *Journal of Biological Chemistry* **282**, 26132–26139 (2007).
9. Gévry, N., Chan, H. M., Laflamme, L., Livingston, D. M. & Gaudreau, L. p21 transcription is regulated by differential localization of histone H2A.Z. *Genes Dev.* **21**, 1869–1881 (2007).
10. Dijkwel, Y. & Tremethick, D. J. The Role of the Histone Variant H2A.Z in Metazoan Development. *Journal of Developmental Biology* **10**, 28 (2022).
11. Johnston, H., Kneer, J., Chackalaparampil, I., Yaciuk, P. & Chrivia, J. Identification of a Novel SNF2/SWI2 Protein Family Member, SRCAP, Which Interacts with CREB-binding Protein*. *Journal of Biological Chemistry* **274**, 16370–16376 (1999).
12. Xu, X. *et al.* Adenovirus DNA Binding Protein Interacts with the SNF2-Related CBP Activator Protein (SrCap) and Inhibits SrCap-Mediated Transcription. *Journal of Virology* **75**, 10033–10040 (2001).
13. Ye, B. *et al.* The chromatin remodeler SRCAP promotes self-renewal of intestinal stem cells. *The EMBO Journal* **39**, e103786 (2020).
14. Creyghton, M. P. *et al.* H2AZ Is Enriched at Polycomb Complex Target Genes in ES Cells and Is Necessary for Lineage Commitment. *Cell* **135**, 649–661 (2008).
15. Ku, M. *et al.* H2A.Z landscapes and dual modifications in pluripotent and multipotent stem cells underlie complex genome regulatory functions. *Genome Biology* **13**, R85 (2012).
16. Murphy, K. E., Meng, F. W., Makowski, C. E. & Murphy, P. J. Genome-wide chromatin accessibility is restricted by ANP32E. *Nat Commun* **11**, 5063 (2020).
17. Berta, D. G. *et al.* Deficient H2A.Z deposition is associated with genesis of uterine leiomyoma. *Nature* **596**, 398–403 (2021).
18. Rudnizky, S., Khamis, H., Malik, O., Melamed, P. & Kaplan, A. The base pair-scale diffusion of nucleosomes modulates binding of transcription factors. *Proceedings of the National Academy of Sciences* **116**, 12161–12166 (2019).
19. Pünzeler, S. *et al.* Multivalent binding of PWWP2A to H2A.Z regulates mitosis and neural crest differentiation. *The EMBO Journal* **36**, 2263–2279 (2017).
20. Mylonas, C., Lee, C., Auld, A. L., Cisse, I. I. & Boyer, L. A. A dual role for H2A.Z.1 in modulating the dynamics of RNA polymerase II initiation and elongation. *Nat Struct Mol Biol* **28**, 435–442 (2021).
21. Wen, Z., Zhang, L., Ruan, H. & Li, G. Histone variant H2A.Z regulates nucleosome unwrapping and CTCF binding in mouse ES cells. *Nucleic Acids Research* **48**, 5939–5952 (2020).
22. Cole, L. *et al.* Multiple roles of H2A.Z in regulating promoter chromatin architecture in human cells. *Nat Commun* **12**, 2524 (2021).

23. Lukauskas, S. *et al.* Decoding chromatin states by proteomic profiling of nucleosome readers. *Nature* **627**, 671–679 (2024).
24. Shen, T. *et al.* Brain-specific deletion of histone variant H2A.z results in cortical neurogenesis defects and neurodevelopmental disorder. *Nucleic Acids Research* **46**, 2290–2307 (2018).
25. Greenberg, R. S., Long, H. K., Swigut, T. & Wysocka, J. Single Amino Acid Change Underlies Distinct Roles of H2A.Z Subtypes in Human Syndrome. *Cell* **178**, 1421-1436.e24 (2019).
26. Zilberman, D., Coleman-Derr, D., Ballinger, T. & Henikoff, S. Histone H2A.Z and DNA methylation are mutually antagonistic chromatin marks. *Nature* **456**, 125–129 (2008).
27. Conerly, M. L. *et al.* Changes in H2A.Z occupancy and DNA methylation during B-cell lymphomagenesis. *Genome Res.* **20**, 1383–1390 (2010).
28. Bagchi, D. N., Battenhouse, A. M., Park, D. & Iyer, V. R. The histone variant H2A.Z in yeast is almost exclusively incorporated into the +1 nucleosome in the direction of transcription. *Nucleic Acids Research* **48**, 157–170 (2020).
29. Bowman, T. A., Wong, M. M., Cox, L. K., Baldassare, J. J. & Chrivia, J. C. Loss of H2A.Z Is Not Sufficient to Determine Transcriptional Activity of Snf2-Related CBP Activator Protein or p400 Complexes. *International Journal of Cell Biology* **2011**, e715642 (2011).
30. Nishimura, K., Fukagawa, T., Takisawa, H., Kakimoto, T. & Kanemaki, M. An auxin-based degron system for the rapid depletion of proteins in nonplant cells. *Nat Methods* **6**, 917–922 (2009).
31. Raccaud, M. *et al.* Mitotic chromosome binding predicts transcription factor properties in interphase. *Nat Commun* **10**, 487 (2019).
32. King, H. W. & Klose, R. J. The pioneer factor OCT4 requires the chromatin remodeller BRG1 to support gene regulatory element function in mouse embryonic stem cells. *eLife* **6**, e22631 (2017).
33. Friman, E. T. *et al.* Dynamic regulation of chromatin accessibility by pluripotency transcription factors across the cell cycle. *eLife* **8**, e50087 (2019).
34. Niwa, H., Miyazaki, J. & Smith, A. G. Quantitative expression of Oct-3/4 defines differentiation, dedifferentiation or self-renewal of ES cells. *Nat Genet* **24**, 372–376 (2000).
35. Pundhir, S. *et al.* The impact of SWI/SNF and NuRD inactivation on gene expression is tightly coupled with levels of RNA polymerase II occupancy at promoters. *Genome Res.* **33**, 332–345 (2023).
36. Ranjan, A. *et al.* Live-cell single particle imaging reveals the role of RNA polymerase II in histone H2A.Z eviction. *eLife* **9**, e55667 (2020).
37. Placzek, S., Vanzan, L. & Suter, D. M. Orchestration of pluripotent stem cell genome reactivation during mitotic exit. 2023.08.09.552605 Preprint at https://doi.org/10.1101/2023.08.09.552605 (2023).
38. Kelly, T. K. *et al.* H2A.Z Maintenance during Mitosis Reveals Nucleosome Shifting on Mitotically Silenced Genes. *Molecular Cell* **39**, 901–911 (2010).
39. Nekrasov, M. *et al.* Histone H2A.Z inheritance during the cell cycle and its impact on promoter organization and dynamics. *Nat Struct Mol Biol* **19**, 1076–1083 (2012).
40. Giaimo, B. D., Ferrante, F., Herchenröther, A., Hake, S. B. & Borggrefe, T. The histone variant H2A.Z in gene regulation. *Epigenetics & Chromatin* **12**, 37 (2019).
41. Palozola, K. C. *et al.* Mitotic transcription and waves of gene reactivation during mitotic exit. *Science* **358**, 119–122 (2017).

42. Gaidatzis, D., Burger, L., Florescu, M. & Stadler, M. B. Analysis of intronic and exonic reads in RNA-seq data characterizes transcriptional and post-transcriptional regulation. *Nat Biotechnol* **33**, 722–729 (2015).
43. Yang, Y. *et al.* HIRA complex presets transcriptional potential through coordinating depositions of the histone variants H3.3 and H2A.Z on the poised genes in mESCs. *Nucleic Acids Research* **50**, 191–206 (2022).
44. Schoenfelder, S. & Fraser, P. Long-range enhancer–promoter contacts in gene expression control. *Nat Rev Genet* **20**, 437–455 (2019).
45. Schneider, J. *et al.* Molecular Regulation of Histone H3 Trimethylation by COMPASS and the Regulation of Gene Expression. *Molecular Cell* **19**, 849–856 (2005).
46. Policarpi, C., Munafò, M., Tsagkris, S., Carlini, V. & Hackett, J. A. Systematic epigenome editing captures the context-dependent instructive function of chromatin modifications. *Nat Genet* 1–13 (2024) doi:10.1038/s41588-024-01706-w.
47. Wang, H. *et al.* H3K4me3 regulates RNA polymerase II promoter-proximal pause-release. *Nature* **615**, 339–348 (2023).
48. Willhoft, O. *et al.* Structure and dynamics of the yeast SWR1-nucleosome complex. *Science* **362**, eaat7716 (2018).
49. Poyton, M. F. *et al.* Coordinated DNA and histone dynamics drive accurate histone H2A.Z exchange. *Science Advances* **8**, eabj5509 (2022).
50. Kubik, S. *et al.* Nucleosome Stability Distinguishes Two Different Promoter Types at All Protein-Coding Genes in Yeast. *Molecular Cell* **60**, 422–434 (2015).
51. Brahma, S. & Henikoff, S. RSC-Associated Subnucleosomes Define MNase-Sensitive Promoters in Yeast. *Molecular Cell* **73**, 238-249.e3 (2019).
52. Jin, C. & Felsenfeld, G. Nucleosome stability mediated by histone variants H3.3 and H2A.Z. *Genes Dev.* **21**, 1519–1529 (2007).
53. Jin, C. *et al.* H3.3/H2A.Z double variant–containing nucleosomes mark 'nucleosome-free regions' of active promoters and other regulatory regions. *Nat Genet* **41**, 941–945 (2009).
54. Xi, Y., Yao, J., Chen, R., Li, W. & He, X. Nucleosome fragility reveals novel functional states of chromatin and poises genes for activation. *Genome Res.* **21**, 718–724 (2011).
55. Bentsen, M. *et al.* ATAC-seq footprinting unravels kinetics of transcription factor binding during zygotic genome activation. *Nat Commun* **11**, 4267 (2020).
56. Lemma, R. B. *et al.* Pioneer transcription factors are associated with the modulation of DNA methylation patterns across cancers. *Epigenetics & Chromatin* **15**, 13 (2022).
57. Peng, Y. *et al.* Detection of new pioneer transcription factors as cell-type-specific nucleosome binders. *eLife* **12**, RP88936 (2024).
58. Ugur, E. *et al.* Comprehensive chromatin proteomics resolves functional phases of pluripotency and identifies changes in regulatory components. *Nucleic Acids Research* **51**, 2671–2690 (2023).
59. Becker, J. S. *et al.* Genomic and Proteomic Resolution of Heterochromatin and Its Restriction of Alternate Fate Genes. *Molecular Cell* **68**, 1023-1037.e15 (2017).
60. Cauchy, P., Koch, F. & Andrau, J.-C. Two possible modes of pioneering associated with combinations of H2A.Z and p300/CBP at nucleosome-occupied enhancers. *Transcription* **8**, 179–184 (2017).
61. Michael, A. K. *et al.* Mechanisms of OCT4-SOX2 motif readout on nucleosomes. *Science* **368**, 1460–1465 (2020).

62. Dodonova, S. O., Zhu, F., Dienemann, C., Taipale, J. & Cramer, P. Nucleosome-bound SOX2 and SOX11 structures elucidate pioneer factor function. *Nature* **580**, 669–672 (2020).
63. Masui, S. *et al.* Pluripotency governed by Sox2 via regulation of Oct3/4 expression in mouse embryonic stem cells. *Nat Cell Biol* **9**, 625–635 (2007).
64. Murphy, P. J., Wu, S. F., James, C. R., Wike, C. L. & Cairns, B. R. Placeholder Nucleosomes Underlie Germline-to-Embryo DNA Methylation Reprogramming. *Cell* **172**, 993-1006.e13 (2018).
65. Spruijt, C. G. *et al.* Dynamic Readers for 5-(Hydroxy)Methylcytosine and Its Oxidized Derivatives. *Cell* **152**, 1146–1159 (2013).
66. Domcke, S. *et al.* Competition between DNA methylation and transcription factors determines binding of NRF1. *Nature* **528**, 575–579 (2015).
67. Azevedo Portilho, N. *et al.* The DNMT1 inhibitor GSK-3484862 mediates global demethylation in murine embryonic stem cells. *Epigenetics & Chromatin* **14**, 56 (2021).
68. Dror, I., Zhou, T., Mandel-Gutfreund, Y. & Rohs, R. Covariation between homeodomain transcription factors and the shape of their DNA binding sites. *Nucleic Acids Research* **42**, 430–441 (2014).
69. Kim, S. *et al.* Probing Allostery Through DNA. *Science* **339**, 816–819 (2013).
70. Yu, J. *et al.* Structural insights into histone exchange by human SRCAP complex. *Cell Discov* **10**, 1–18 (2024).
71. Park, G., Patel, A. B., Wu, C. & Louder, R. K. Structures of H2A.Z-associated human chromatin remodelers SRCAP and TIP60 reveal divergent mechanisms of chromatin engagement. Preprint at https://doi.org/10.1101/2024.07.30.605802 (2024).
72. Jalal, A. S. B. *et al.* Stabilization of the hexasome intermediate during histone exchange by yeast SWR1 complex. *Molecular Cell* **84**, 3871-3884.e9 (2024).
73. Louder, R. K. *et al.* Molecular basis of global promoter sensing and nucleosome capture by the SWR1 chromatin remodeler. *Cell* **187**, 6849-6864.e18 (2024).
74. Hong, L. & Lei, J. Scaling law for the radius of gyration of proteins and its dependence on hydrophobicity. *Journal of Polymer Science Part B: Polymer Physics* **47**, 207–214 (2009).
75. Maeshima, K. *et al.* The physical size of transcription factors is key to transcriptional regulation in chromatin domains. *J. Phys.: Condens. Matter* **27**, 064116 (2015).
76. Girvan, P. *et al.* Nucleosome flipping drives kinetic proofreading and processivity by SWR1. *Nature* **636**, 251–257 (2024).
77. Kuhn, T. *et al.* Single-molecule tracking of Nodal and Lefty in live zebrafish embryos supports hindered diffusion model. *Nat Commun* **13**, 6101 (2022).
78. Kuhn, T., Hettich, J., Davtyan, R. & Gebhardt, J. C. M. Single molecule tracking and analysis framework including theory-predicted parameter settings. *Sci Rep* **11**, 9465 (2021).
79. Reisser, M. *et al.* Inferring quantity and qualities of superimposed reaction rates from single molecule survival time distributions. *Sci Rep* **10**, 1758 (2020).
80. Hettich, J. & Gebhardt, J. C. M. Transcription factor target site search and gene regulation in a background of unspecific binding sites. *Journal of Theoretical Biology* **454**, 91–101 (2018).
81. Huynh, D. *et al.* Effective in vivo binding energy landscape illustrates kinetic stability of RBPJ-DNA binding. *Nat Commun* **16**, 1259 (2025).

82. McNally, J. G., Müller, W. G., Walker, D., Wolford, R. & Hager, G. L. The Glucocorticoid Receptor: Rapid Exchange with Regulatory Sites in Living Cells. *Science* **287**, 1262–1265 (2000).
83. Gebhardt, J. C. M. *et al.* Single-molecule imaging of transcription factor binding to DNA in live mammalian cells. *Nat Methods* **10**, 421–426 (2013).
84. Morisaki, T., Müller, W. G., Golob, N., Mazza, D. & McNally, J. G. Single-molecule analysis of transcription factor binding at transcription sites in live cells. *Nat Commun* **5**, 4456 (2014).
85. Schick, S. *et al.* Acute BAF perturbation causes immediate changes in chromatin accessibility. *Nat Genet* **53**, 269–278 (2021).
86. Iurlaro, M. *et al.* Mammalian SWI/SNF continuously restores local accessibility to chromatin. *Nat Genet* **53**, 279–287 (2021).
87. Lashgari, A., Millau, J.-F., Jacques, P.-É. & Gaudreau, L. Global inhibition of transcription causes an increase in histone H2A.Z incorporation within gene bodies. *Nucleic Acids Research* **45**, 12715–12722 (2017).
88. Brahma, S. & Henikoff, S. The BAF chromatin remodeler synergizes with RNA polymerase II and transcription factors to evict nucleosomes. *Nat Genet* **56**, 100–111 (2024).
89. Kaur, U., Muñoz, E. N. & Narlikar, G. J. Hexasomal particles: consequence or also consequential? *Current Opinion in Genetics & Development* **85**, 102163 (2024).
90. Hoffman, J. A., Trotter, K. W. & Archer, T. K. RNA polymerase II coordinates histone deacetylation at active promoters. *Science Advances* **11**, eadt3037 (2025).
91. Chen, Z. *et al.* High-resolution and high-accuracy topographic and transcriptional maps of the nucleosome barrier. *eLife* **8**, e48281 (2019).
92. de Dieuleveult, M. *et al.* Genome-wide nucleosome specificity and function of chromatin remodellers in ES cells. *Nature* **530**, 113–116 (2016).
93. Hon, G. C. *et al.* 5mC Oxidation by Tet2 Modulates Enhancer Activity and Timing of Transcriptome Reprogramming during Differentiation. *Molecular Cell* **56**, 286–297 (2014).
94. Deluz, C. *et al.* A role for mitotic bookmarking of SOX2 in pluripotency and differentiation. *Genes Dev.* **30**, 2538–2550 (2016).
95. Schindelin, J. *et al.* Fiji: an open-source platform for biological-image analysis. *Nat Methods* **9**, 676–682 (2012).
96. Dobin, A. *et al.* STAR: ultrafast universal RNA-seq aligner. *Bioinformatics* **29**, 15–21 (2013).
97. Zhang, Y. *et al.* Model-based Analysis of ChIP-Seq (MACS). *Genome Biology* **9**, R137 (2008).
98. Ramírez, F., Dündar, F., Diehl, S., Grüning, B. A. & Manke, T. deepTools: a flexible platform for exploring deep-sequencing data. *Nucleic Acids Research* **42**, W187–W191 (2014).
99. Neph, S. *et al.* BEDOPS: high-performance genomic feature operations. *Bioinformatics* **28**, 1919–1920 (2012).
100. Quinlan, A. R. & Hall, I. M. BEDTools: a flexible suite of utilities for comparing genomic features. *Bioinformatics* **26**, 841–842 (2010).
101. Li, H. *et al.* The Sequence Alignment/Map format and SAMtools. *Bioinformatics* **25**, 2078–2079 (2009).
102. Chen, K. *et al.* DANPOS: Dynamic analysis of nucleosome position and occupancy by sequencing. *Genome Res.* **23**, 341–351 (2013).

103. Pedersen, B. S., Eyring, K., De, S., Yang, I. V. & Schwartz, D. A. Fast and accurate alignment of long bisulfite-seq reads. Preprint at http://arxiv.org/abs/1401.1129 (2014).
104. Akalin, A. *et al.* methylKit: a comprehensive R package for the analysis of genome-wide DNA methylation profiles. *Genome Biology* **13**, R87 (2012).
105. Love, M. I., Huber, W. & Anders, S. Moderated estimation of fold change and dispersion for RNA-seq data with DESeq2. *Genome Biology* **15**, 550 (2014).
106. Robinson, M. D., McCarthy, D. J. & Smyth, G. K. edgeR: a Bioconductor package for differential expression analysis of digital gene expression data. *Bioinformatics* **26**, 139–140 (2010).
107. Ritchie, M. E. *et al.* limma powers differential expression analyses for RNA-sequencing and microarray studies. *Nucleic Acids Research* **43**, e47 (2015).
108. Yu, G., Wang, L.-G., Han, Y. & He, Q.-Y. clusterProfiler: an R Package for Comparing Biological Themes Among Gene Clusters. *OMICS: A Journal of Integrative Biology* **16**, 284–287 (2012).
109. Wickham, H. *Ggplot2: Elegant Graphics for Data Analysis*. (Springer, New York, NY, 2009). doi:10.1007/978-0-387-98141-3.
110. Durinck, S. *et al.* BioMart and Bioconductor: a powerful link between biological databases and microarray data analysis. *Bioinformatics* **21**, 3439–3440 (2005).
111. Bailey, T. L. & Grant, C. E. SEA: Simple Enrichment Analysis of motifs. 2021.08.23.457422 Preprint at https://doi.org/10.1101/2021.08.23.457422 (2021).
112. Mitternacht, S. FreeSASA: An open source C library for solvent accessible surface area calculations. Preprint at https://doi.org/10.12688/f1000research.7931.1 (2016).
113. Dull, T. *et al.* A Third-Generation Lentivirus Vector with a Conditional Packaging System. *Journal of Virology* **72**, 8463–8471 (1998).
114. Suter, D. M. *et al.* Rapid Generation of Stable Transgenic Embryonic Stem Cell Lines Using Modular Lentivectors. *Stem Cells* **24**, 615–623 (2006).
115. Concordet, J.-P. & Haeussler, M. CRISPOR: intuitive guide selection for CRISPR/Cas9 genome editing experiments and screens. *Nucleic Acids Research* **46**, W242–W245 (2018).
116. Egan, B. *et al.* An Alternative Approach to ChIP-Seq Normalization Enables Detection of Genome-Wide Changes in Histone H3 Lysine 27 Trimethylation upon EZH2 Inhibition. *PLOS ONE* **11**, e0166438 (2016).
117. Patty, B. J. & Hainer, S. J. Widespread impact of nucleosome remodelers on transcription at cis-regulatory elements. 2024.04.12.589208 Preprint at https://doi.org/10.1101/2024.04.12.589208 (2024).
118. Buenrostro, J. D., Giresi, P. G., Zaba, L. C., Chang, H. Y. & Greenleaf, W. J. Transposition of native chromatin for fast and sensitive epigenomic profiling of open chromatin, DNA-binding proteins and nucleosome position. *Nat Methods* **10**, 1213–1218 (2013).
119. Picelli, S. *et al.* Tn5 transposase and tagmentation procedures for massively scaled sequencing projects. *Genome Res.* **24**, 2033–2040 (2014).
120. Esnault, C., Magat, T., García-Oliver, E. & Andrau, J.-C. Analyses of PromoterPromoters, Enhancer, and NucleosomeNucleosomesOrganization in Mammalian Cells by MNase-Seq. in *Enhancers and Promoters: Methods and Protocols* (eds. Borggrefe, T. & Giaimo, B. D.) 93–104 (Springer US, New York, NY, 2021). doi:10.1007/978-1-0716-1597-3_5.
121. Tokunaga, M., Imamoto, N. & Sakata-Sogawa, K. Highly inclined thin illumination enables clear single-molecule imaging in cells. *Nat Methods* **5**, 159–161 (2008).

122. Mazza, D., Abernathy, A., Golob, N., Morisaki, T. & McNally, J. G. A benchmark for chromatin binding measurements in live cells. *Nucleic Acids Research* **40**, e119 (2012).
123. Shaban, H. A., Barth, R., Recoules, L. & Bystricky, K. Hi-D: nanoscale mapping of nuclear dynamics in single living cells. *Genome Biology* **21**, 95 (2020).
124. Chen, J. *et al.* Single-Molecule Dynamics of Enhanceosome Assembly in Embryonic Stem Cells. *Cell* **156**, 1274–1285 (2014).
125. Loffreda, A. *et al.* Live-cell p53 single-molecule binding is modulated by C-terminal acetylation and correlates with transcriptional activity. *Nat Commun* **8**, 313 (2017).
126. Tang, X. *et al.* Kinetic principles underlying pioneer function of GAGA transcription factor in live cells. *Nat Struct Mol Biol* **29**, 665–676 (2022).
127. Huynh, D. *et al.* Effective in vivo binding energy landscape illustrates kinetic stability of RBPJ-DNA binding. 2023.12.19.572376 Preprint at https://doi.org/10.1101/2023.12.19.572376 (2024).
128. Gao, T. & Qian, J. EnhancerAtlas 2.0: an updated resource with enhancer annotation in 586 tissue/cell types across nine species. *Nucleic Acids Research* **48**, D58–D64 (2020).
129. Lee, S. *et al.* Covering all your bases: incorporating intron signal from RNA-seq data. *NAR Genomics and Bioinformatics* **2**, lqaa073 (2020).
130. Liao, Y., Smyth, G. K. & Shi, W. featureCounts: an efficient general purpose program for assigning sequence reads to genomic features. *Bioinformatics* **30**, 923–930 (2014).
131. Eisenberg, E. & Levanon, E. Y. Human housekeeping genes, revisited. *Trends in Genetics* **29**, 569–574 (2013).
132. Castro-Mondragon, J. A. *et al.* JASPAR 2022: the 9th release of the open-access database of transcription factor binding profiles. *Nucleic Acids Research* **50**, D165–D173 (2022).
133. Pomaznoy, M., Ha, B. & Peters, B. GOnet: a tool for interactive Gene Ontology analysis. *BMC Bioinformatics* **19**, 470 (2018).

Extended data

Supplementary Figures

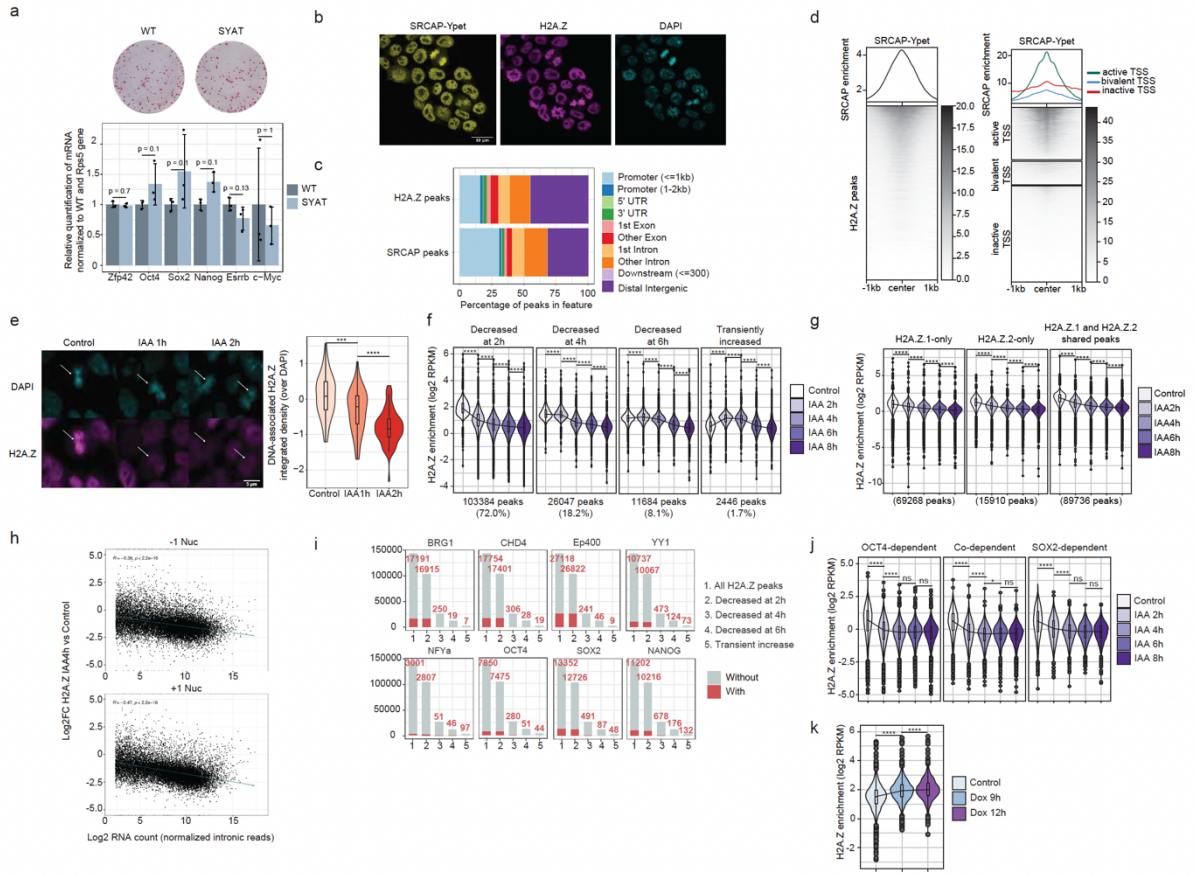

Fig.S1: Related to Fig.1. **a**, Validation of pluripotency of SYAT cells. Top: Alkaline Phosphatase staining of wt and SYAT mESCs. Bottom: Quantification of pluripotency TF expression by RT-qPCR in wt and SYAT mESCs. N=3. p-values were determined by a Kruskal-Wallis test. **b**, Microscopy snapshot of SYAT cells stained with an anti-H2A.Z antibody and DAPI. **c**, SRCAP and H2A.Z peak enrichment by genomic locus type. **d**, SRCAP enrichment determined by CUT&Tag with an anti-GFP antibody at H2A.Z peaks (left) or TSS (right) **e**, Left: Microscopy snapshots of SYAT cells treated with control or IAA for 2 h and stained with anti-H2A.Z antibody and DAPI. White arrows: mitotic cells. Right: Quantification of DNA-associated H2A.Z normalized on DAPI in mitotic cells treated with IAA or control. N = 50 cells per condition. **f**, Classification of H2A.Z-enriched regions as a function of H2A.Z turnover rate. **g**, H2A.Z enrichment in SYAT cells treated with control or IAA for 2, 4, 6, or 8 h, at genomic regions enriched for H2A.Z.1, H2A.Z.2 or both. **h**, Changes of H2A.Z levels at the -1 and +1 nucleosomes, between 0 and 4 h of IAA treatment, as a function of intronic reads of the downstream genes in the absence of IAA. **i**, Total (gray) or enriched (red) peaks for BRG1, CHD4 and Ep400 in the different clusters defined in (**d**). **j**, H2A.Z enrichment at regions depending on OCT4 or SOX2 for their accessibility. p-values were determined by a pairwise Wilcoxon test, *: p<0.05, ****: p<0.0001, ns: non-significant. **k**, H2A.Z enrichment upon OCT4 knockdown in ZHBTc4 treated with Doxycycline for 9 or 12 h. ****: p<0.0001, *: p<0.05, ns: non-significant. Boxes and outlier points are represented as in Fig.1e.

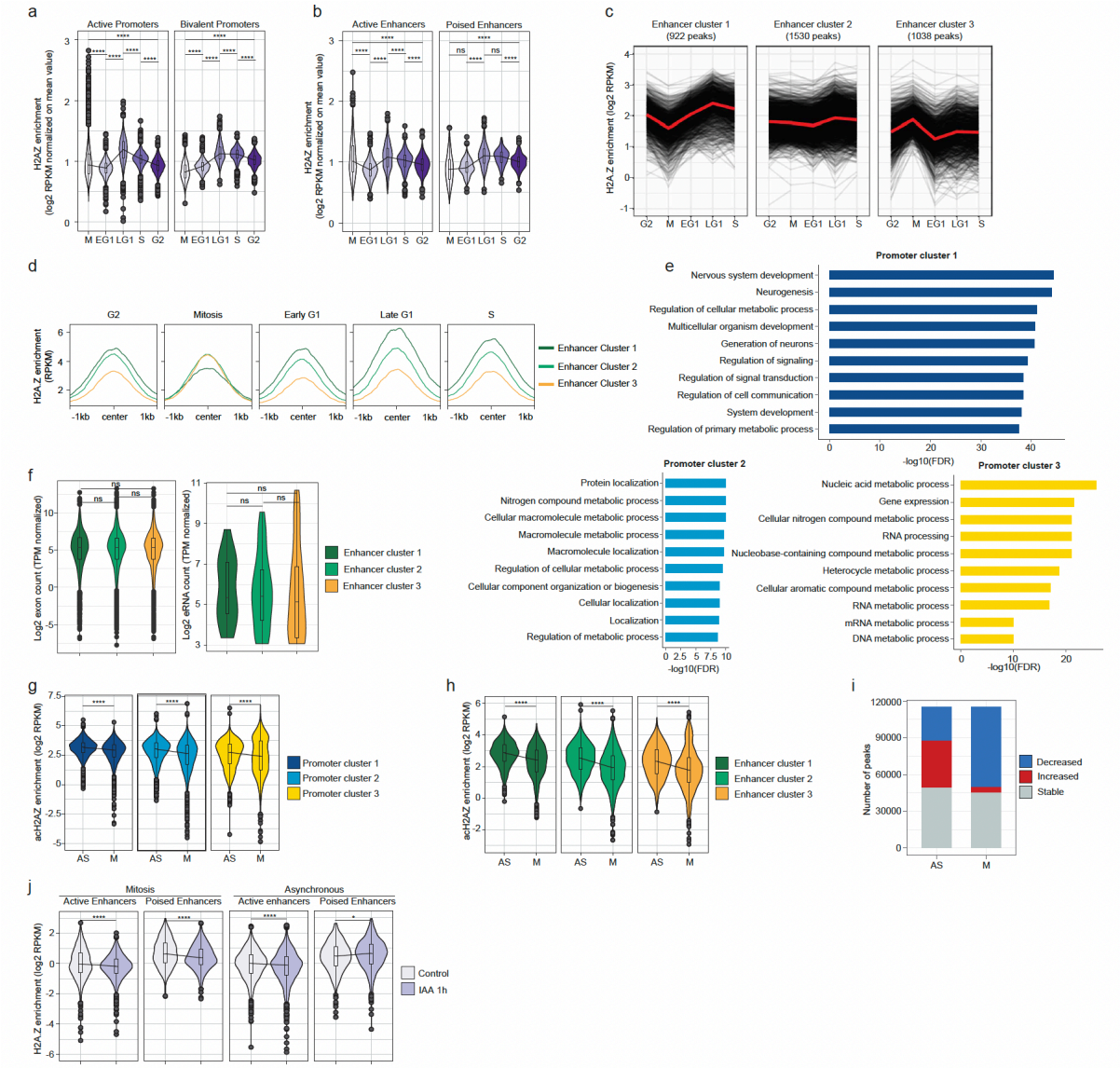

Fig.S2: Related to Fig.2. **a** and **b**, Mean-normalized scores of each H2A.Z peak calculated from H2A.Z scores across the cell cycle in promoters (**a**) and enhancers (**b**). **c**, H2A.Z enrichment in enhancer peaks with decreased, stable or increased mitotic H2A.Z levels with respect to G2 and EG1 phases. **d**, H2A.Z enrichment around H2A.Z peaks in the clusters defined in (**b**). **e**, Top-ten enriched GO terms in mitotic promoter clusters. **f**, Intronic counts of genes regulated by each of the three enhancer clusters (left) and enhancer RNA counts (right) of the enhancers belonging to the three mitotic clusters. **g** and **h**, AcH2A.Z enrichment in asynchronous and mitotic cells in mitotic promoter (**g**) and enhancer (**h**) clusters. **i**, Numbers of peaks displaying increased, stable or decreased H2A.Z score after 1 h of IAA treatment in asynchronous or mitotic cells. **j**, H2A.Z enrichment at enhancers in mitotic or asynchronous SYAT cells treated for 1 h with IAA. p-values were determined by a pairwise Wilcoxon test, ****: p<0.0001, ***: p<0.001, **: p<0.01, *: p<0.05, ns: non-significant.

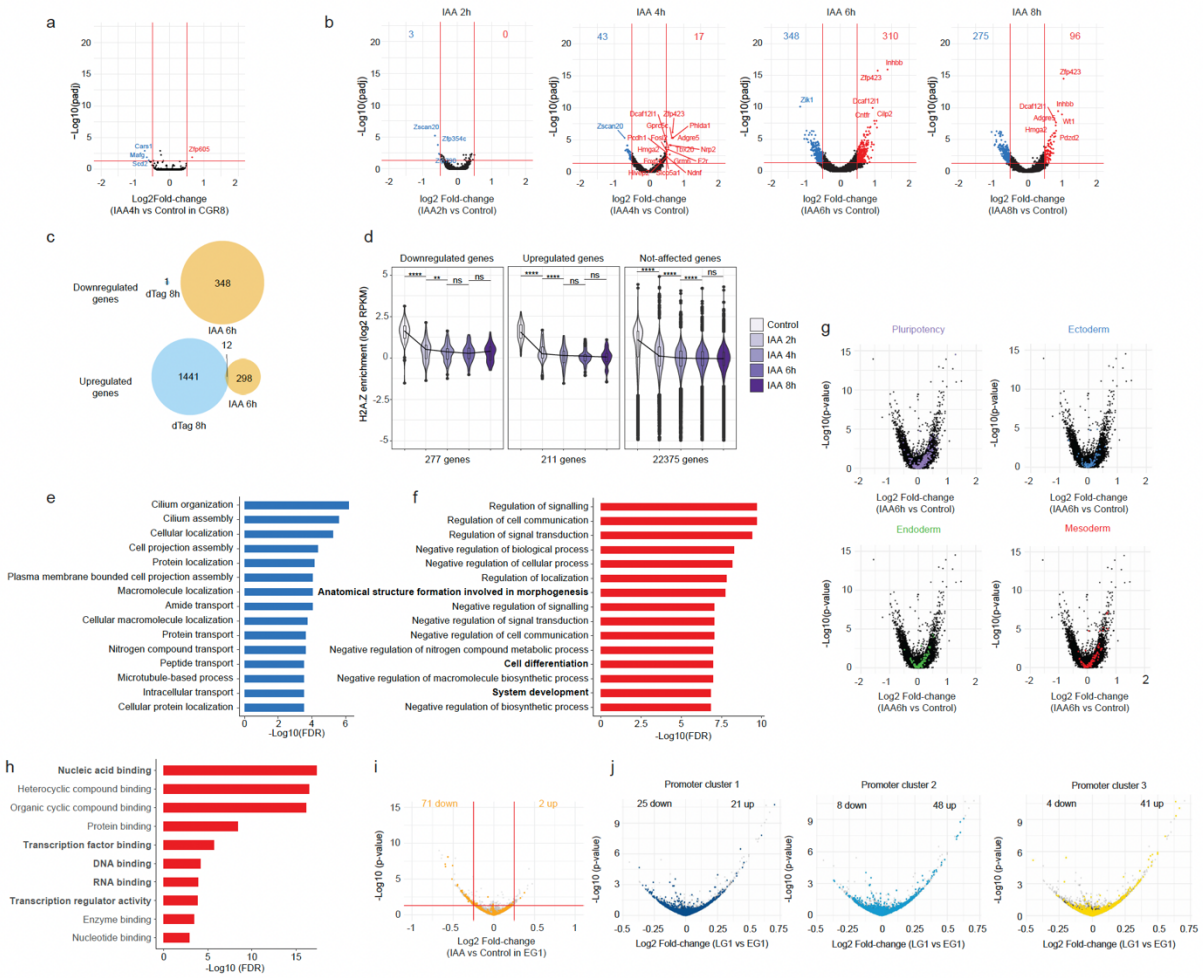

Fig.S3: Related to Fig.3. **a**, Fold-change of intronic reads and adjusted p-value, for wt cells treated for 4 h with IAA. **b**, Fold-change of exonic reads and adjusted p-value, for SYAT cells treated 2, 4, 6 and 8 h with IAA. Numbers: genes significantly downregulated (blue) or upregulated (red) with a threshold of |log2FC|>0.5 and adjusted p-value < 0.05. **c**, Genes overlapping between those significantly affected after 6 h of IAA treatment and genes affected after 8 h of H2A.Z.1 depletion in [20] when analyzing exonic reads. **d**, H2A.Z enrichment (Log2 RPKM) determined by ChIP-Seq, at promoters of upregulated or downregulated genes after 6 h of IAA treatment, or unaffected genes over the course of 8 h of IAA treatment. p-values were determined by a pairwise Wilcoxon test; ****: p<0.0001; **: p<0.01; ns: non-significant. **e** and **f**, Top 15 GO terms enriched for downregulated (**e**) or upregulated (**f**) genes after 6 h of IAA treatment in the "cellular process" category. **g**, Fold-change of intronic reads and adjusted p-value for SYAT cells treated for 6 h with IAA. Genes associated with pluripotency or commitment to the three germ layers are colored. **h**, Top-ten enriched GO terms for molecular functions, in proteins increased in the proteome upon 4 h of IAA treatment. **i**, Fold-change of intronic reads for SYAT cells treated for 1 h with IAA and sorted in early G1. Housekeeping genes are colored in orange. Numbers: housekeeping genes significantly downregulated or upregulated with a threshold of |log2FC|>0.25 and p-value < 0.05. **j**, Fold-change of intronic reads for control SYAT cells in LG1 versus EG1, genes are colored according to promoter clusters defined in Fig.2c.

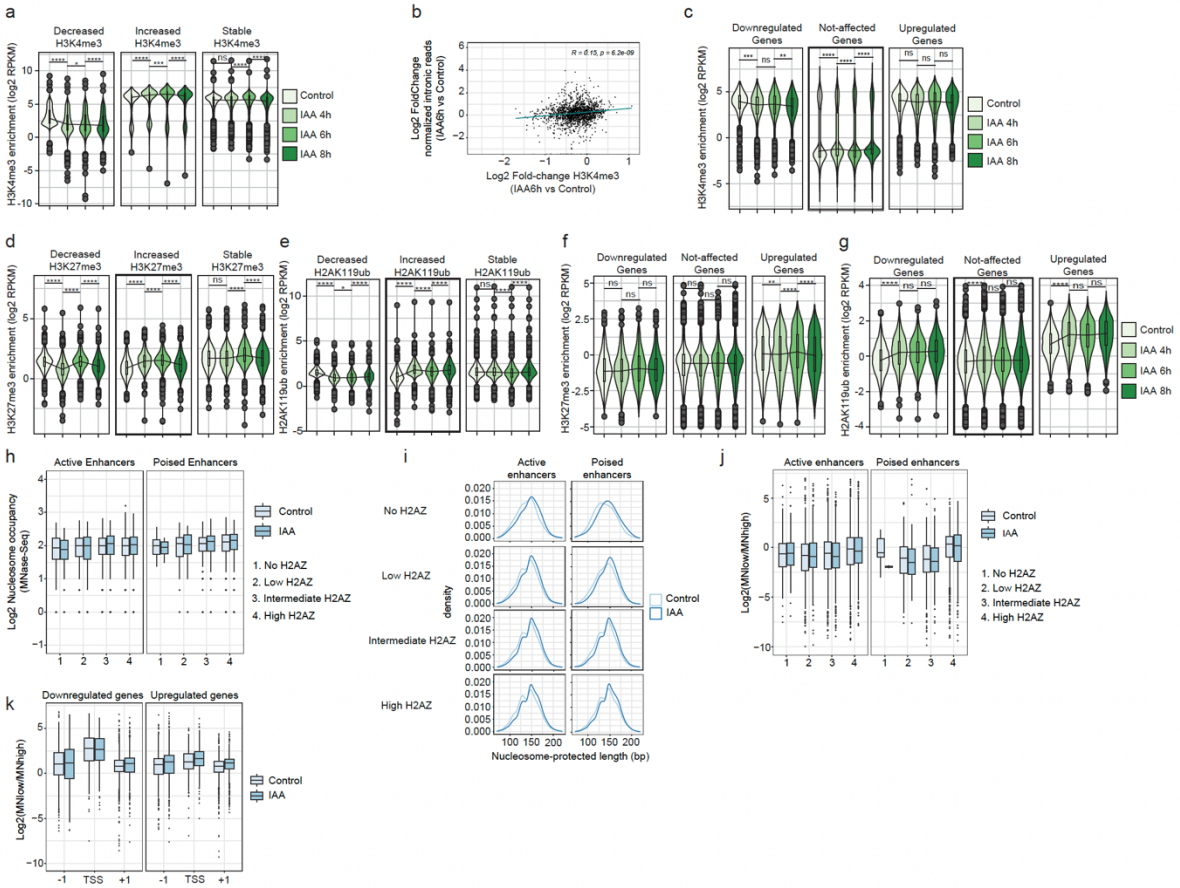

Fig.S4: Related to Fig.4. **a**, Enrichment of H3K4me3 in SYAT cells treated with control or IAA for 4, 6 and 8 h. **b**, Changes in intronic reads of genes controlled by a bivalent promoter as a function of H3K4me3 enrichment between 6 h of IAA treatment and control. Upper right corner: Pearson correlation coefficient. **c**, H3K4me3 enrichment in SYAT cells treated with control or IAA for 4, 6 and 8 h, at promoters of genes downregulated or upregulated upon SRCAP depletion. **d** and **e**, Enrichment of H3K27me3 (d) and H2AK119ub1 (e) in SYAT cells treated with control or IAA for 4, 6 and 8 h. **f** and **g**, H3K27me3 (**f**) and H2AK119ub1 (**g**) enrichment in SYAT cells treated with control or IAA for 4, 6 and 8 h, at promoters of genes downregulated or upregulated upon SRCAP depletion. **h**, Nucleosome occupancy at enhancers in SYAT cells as a function of H2A.Z levels, in control or after 4 h of IAA treatment. **i**, MNase-Seq fragment densities in SYAT cells treated or not with IAA for 4 h as a function of H2A.Z enrichment and enhancer type. **j**, Fragile nucleosomes located at different types of enhancers, as a function of H2A.Z levels. **k**, Fragile nucleosomes at -1, TSS and +1 nucleosomes of genes downregulated and upregulated upon SRCAP degradation. p-values were determined by a pairwise Wilcoxon test; ****: p<0.0001; **: p<0.01; *: p<0.05, ns: non-significant.

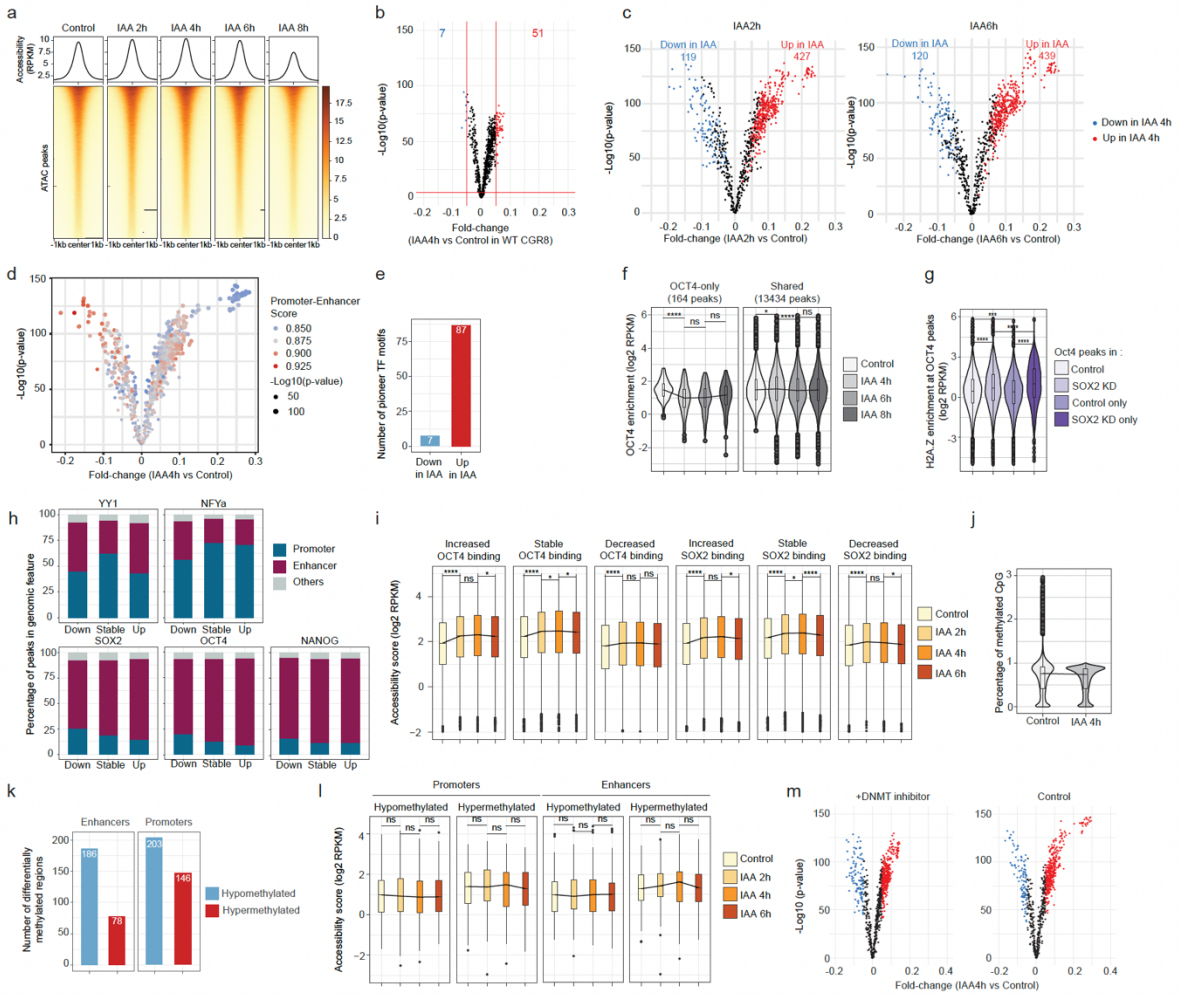

Fig.S5: Related to Fig.5. **a**, Heatmap of chromatin accessibility determined by ATAC-Seq and centered on the summit of accessible peaks, in SYAT cells upon IAA treatment for 2, 4, 6 and 8 h. **b**, Fold-change of TF footprinting calculated using TOBIAS in wt CGR8 cells treated with control or IAA. Colors represent TF motifs predicted to lose (in blue) or gain (in red) binding upon IAA treatment in CGR8 cells with a threshold of |FC|>0.05 and p-value < 0.0001. **c**, Fold-change of TF footprinting calculated using TOBIAS in SYAT cells treated 2 h (left panel) or 6 h (right panel) with IAA versus control. Colors: TF motifs predicted to lose (blue) or gain (red) binding upon 4 h-IAA treatment with a threshold of |FC|>0.05 and p-value < 0.0001. **d**, Fold-change of TF footprinting calculated using TOBIAS in SYAT cells treated 4 h with IAA versus control. Color scale: promoter-enhancer score; dot size: -log10(p-value). **e**, Number of binding motifs of pTFs, among motifs predicted to lose or gain binding upon 4 h of IAA treatment. **f**, OCT4 ChIP-seq enrichment score at peaks bound by OCT4 only or shared with SOX2 in SYAT cells treated with IAA for 4, 6 and 8 h or control. **g**, H2A.Z enrichment score in 2TS22C cells, at all peaks bound by OCT4 in control conditions, upon SOX2 knockdown, or at peaks unique to control or SOX2 knockdown conditions. **h**, Percentage of peaks where TFs increase, decrease or maintain a stable binding upon IAA treatment, in promoters or enhancers. **i**, Accessibility changes upon IAA treatment at peaks gaining, losing or maintaining binding of OCT4 or SOX2. Black line: changes in median values. Boxes: interquartile range, dots: outlier points. **j**, Percentage of methylated cytosines in H2A.Z peaks in SYAT cells treated with control or IAA. **k**, Number of promoters or enhancers with cytosine hyper- or hypomethylation upon 4 h of IAA treatment. **l**, Chromatin accessibility changes upon IAA treatment at hyper- or hypomethylated promoters and enhancers. **m**, Fold-change of TF footprinting calculated using TOBIAS, in SYAT cells treated or not for 5 days with a DNMT1 inhibitor and treated 4 h with IAA versus control. p-values were determined by a pairwise Wilcoxon test; ****: p<0.0001; ***: p<0.001; *: p<0.05, ns: non-significant.

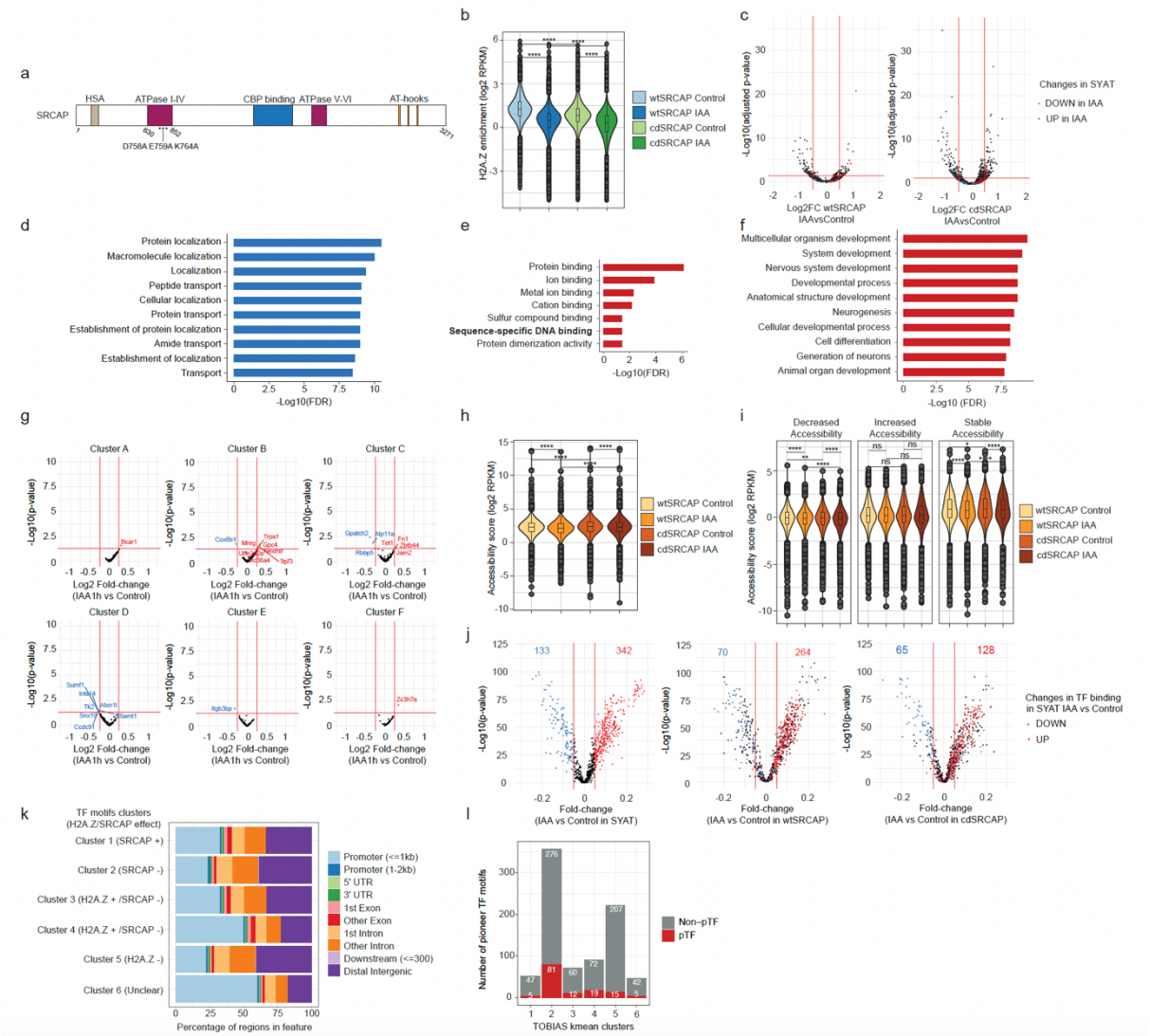

Fig.S6: Related to Fig.6. **a**, Schematic representation of the SRCAP protein with its functional domains. Stars: mutations introduced in the ATPase domain of SRCAP. **b**, H2A.Z enrichment determined by ChIP-Seq in all H2A.Z peaks upon overexpression of wtSRCAP or cdSRCAP and treated with control or IAA for 4 h. **c**, Fold-change in intronic reads in wtSRCAP (left panel) or cdSRCAP (right panel) treated with control or IAA for 4 h. Colors: intronic read changes observed in SYAT cells after 4 h of IAA treatment. **d**, Top 10 GO terms in the "cellular process" category, enriched for genes in cluster D and E defined in Fig.6c. **e**, Top 10 GO terms in the "molecular function" category, enriched for genes upregulated in cdSRCAP IAA compared to wtSRCAP IAA. **f**, Top 10 GO terms in the "cellular process" category, enriched for genes upregulated in cdSRCAP IAA compared to wtSRCAP IAA. **g**, Fold-change in intronic reads in the 6 clusters defined in Fig.6f for SYAT cells treated for 1 h with IAA or control and FACSorted in LG1. **h**, Chromatin accessibility changes in all accessible peaks upon overexpression of wtSRCAP or cdSRCAP and treated with control or IAA for 4 h. **i**, Chromatin accessibility changes upon overexpression of wtSRCAP or cdSRCAP and treated with control or IAA for 4 h, in peaks gaining, losing, or maintaining accessibility in SYAT cells upon 4 h of IAA treatment. **j**, Fold-change of TF footprinting in regions rescued for H2A.Z levels calculated using TOBIAS in SYAT, wtSRCAP and cdSRCAP cells treated with control or IAA for 4 h. Colored dots: motifs predicted to gain or lose binding in rescued regions in SYAT cells treated with IAA versus control. Numbers: Motifs significantly up or down in SYAT and that are still up or down in wtSRCAP or cdSRCAP. **k**, Percentage of motif occurrence, belonging to the six clusters determined in

Fig.6h, in different types of genomic regions. **I**, Number of binding motifs of pioneer TFs in the six motif clusters determined in Fig.6h.

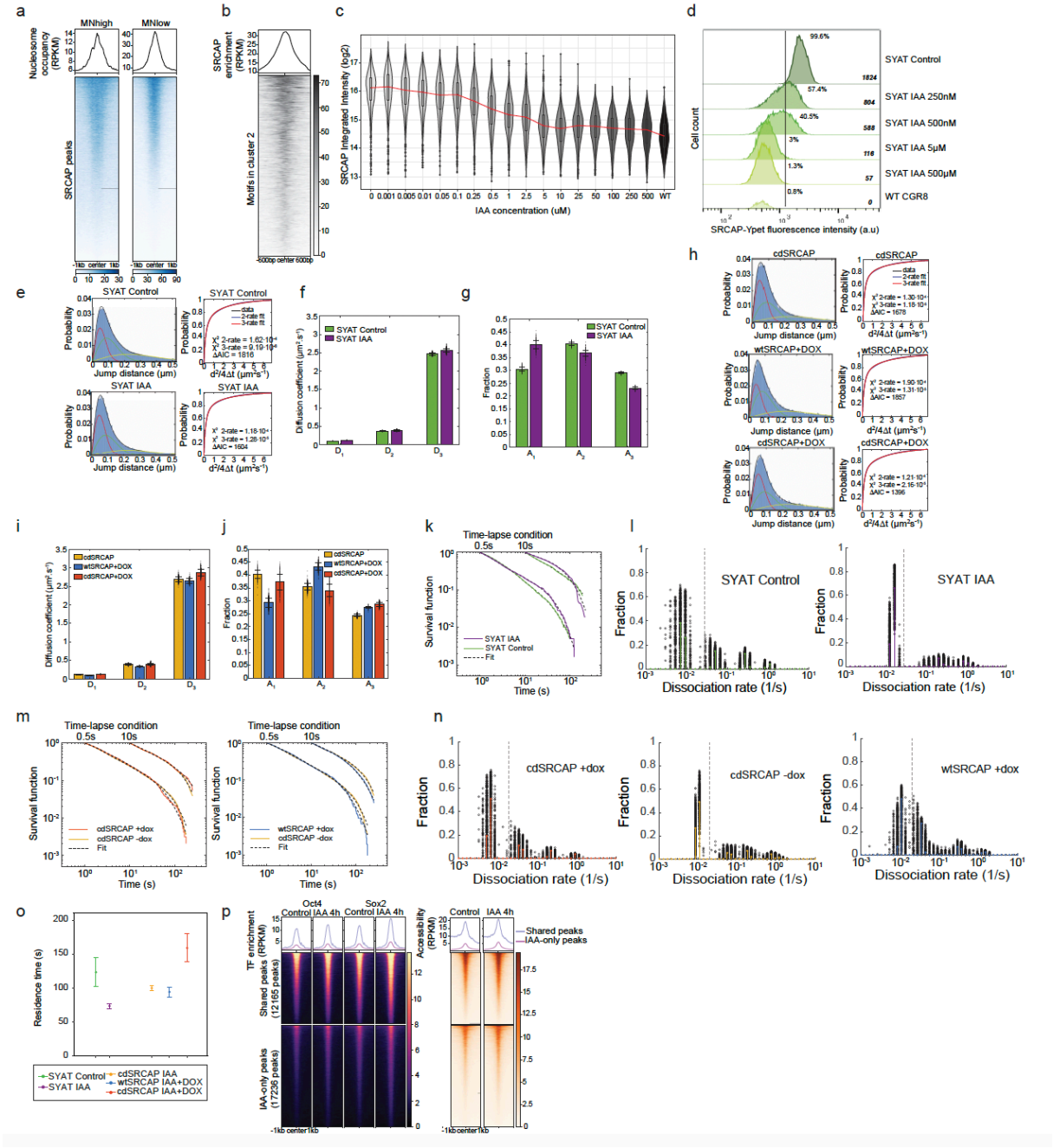

Fig.S7: Related to Fig.7. **a,** Nucleosome occupancy at SRCAP peaks, determined by MNase-Seq using either high (left) or low (right) concentration of MNase. **b,** SRCAP enrichment assessed by CUT&RUN in a 1.2kb region centered around TF motifs belonging to cluster 2 (Fig.6c). **c,** Quantification of SRCAP-Ypet fluorescence intensity after background subtraction by live-imaging in SYAT cells treated for 2h with different doses of IAA or CTRL. **d,** SRCAP-Ypet fluorescence intensity determined by Flow Cytometry analysis of SYAT cells treated for 2h with different doses of IAA or CTRL. Percentage of Ypet positive cells as well as mean intensity after subtraction of Ypet intensity in WT CGR8 cells are indicated. **e,** Jump distance distributions (left) and cumulative jump distance distributions (right) of Halo-NANOG in CTRL or after 4h IAA treatment. Jump distance distributions are overlayed with a three-component

diffusion model (black) and the three single components (red, green, yellow). Cumulative jump distance distributions show data (black line) fitted with a 2-component (blue) and a 3-component (red) diffusion model. The insets give values for reduced χ^2 and Akaike Information Criterion (AIC), revealing the better suitability of the 3-component fit. CTRL: 29891 tracks in 25 cells, IAA: 14294 tracks in 22 cells. **f** and **g,** Diffusion coefficients (f) and fractions (g) of three-component diffusion model fitted to (e). Data represent mean values ± s.d. from 400 resamplings with randomly selected 80 % of the data. **h,** Jump distance distributions (left) and cumulative jump distance distributions (right) of Halo-NANOG upon IAA treatment in cdSRCAP cells, wtSRCAP cells treated with Dox and in cdSRCAP cells treated with Dox. Data displayed as in e. wtSRCAP+dox: 6807 tracks in 11 cells, cdSRCAP +dox: 7207 tracks in 19 cells, cdSRCAP-dox: 9244 tracks in 34 cells. **i** and **j,** Diffusion coefficients (i) and fractions (j) of three-component diffusion model fitted to (h). Data represent mean values ± s.d. from 400 resamplings with randomly selected 80 % of the data. **k,** Survival time distributions of Halo-NANOG in SYAT CTRL (green) or treated with IAA (purple) at time-lapse conditions shown on top and survival time functions obtained with GRID (black dashed lines). IAA: 1121 tracks in 26 cells, CTRL: 2813 tracks in 16 cells. **l,** State spectra of dissociation rates obtained with GRID from distributions in (k) using all data for Halo-NANOG in SYAT CTRL (green, left panel) or treated with IAA (purple, right panel). As an error estimation GRID was run 500 times with each run using 80 % of the data (black circles). The dashed lines indicate a dissociation rate of 0.02 s^{-1}. **m,** Survival time distributions of Halo-NANOG in cdSRCAP cells +dox (red), in cdSRCAP cells -dox (yellow) and in wtSRCAP cells +dox (blue) at time-lapse conditions shown on top and survival time functions obtained with GRID (black lines). cdSRCAP+dox: 1623 tracks in 16 cells, cdSRCAP-dox: 4624 tracks in 47 cells, wtSRCAP+dox: 2571 tracks in 34 cells. **n,** State spectra of dissociation rates obtained with GRID from distributions in (m) using all data for Halo-NANOG in cdSRCAP cells +dox (red, left panel), in cdSRCAP cells -dox (yellow, middle panel), and in wtSRCAP cells +dox (blue, right panel). As an error estimation GRID was run 500 times with each run using 80 % of the data (black circles). The dashed lines indicate a dissociation rate of 0.02 s^{-1}. **o,** Average residence time of Halo-NANOG molecules bound longer than 50s, calculated from data displayed in fig.S7-l,n, with the statistics provided there. Error bars denote s.d. of 500 resamplings with randomly selected 80 % of the data and error propagation. **p,** Enrichment of OCT4 and SOX2 (left panel) and accessibility score determined by ATAC-Seq in SYAT cells treated with CTRL or IAA for 4 hours at NANOG peaks shared between CTRL and IAA condition or unique to 4 hour-IAA treatment.

Table S4. List of primers used in the study

Primer Name	Source or reference	Sequence	Application
Rps5 Fw	This paper	TGGCAGAGACCCCTGACAT	RTqPCR
Rps5 Rev	This paper	GGGCAGGTACTTGGCATACT	RTqPCR
Zfp42 Fw	This paper	CCCTCGACAGACTGACCCTAA	RTqPCR
Zfp42 Rev	This paper	TCGGGGCTAATCTCACTTTCAT	RTqPCR
Pou5f1 Fw	This paper	GAGGAGTCCCAGGACATGAA	RTqPCR
Pou5f1 Rev	This paper	AGATGGTGGTCTGGCTGAAC	RTqPCR
Sox2 Fw	This paper	GCACATGAACGGCTGGAGCAACG	RTqPCR
Sox2 Rev	This paper	TGCTGCGAGTAGGACATGCTGTAGG	RTqPCR
Nanog Fw	This paper	AACCAAAGGATGAAGTGCAAGCGG	RTqPCR
Nanog Rev	This paper	TCCAAGTTGGGTTGGTCCAAGTCT	RTqPCR
Esrrb Fw	This paper	CCGATTTCCCCACCTGCTAA	RTqPCR
Esrrb Rev	This paper	GGCCCAGTTGATGAGGAACA	RTqPCR
c-Myc Fw	This paper	GAGCTCCTCGAGCTGTTTGA	RTqPCR
c-Myc rev	This paper	GCATCGTCGTGGCTGTCT	RTqPCR
SRCAP gRNA Fw	This paper	CACCGCGAAAGGCCAAGACGTGAat	gRNA
SRCAP gRNA rev	This paper	AAACatTCACGTCTTGGCCTTTCGC	gRNA
SRCAP homology arms Fw	This paper	cccacctatgtatccctactattagtcacagaggtcgaaaggccaagacgGGTGGCGGTGGATCCGGAG	PCR of KI cassette
SRCAP homology arms Rev	This paper	gcaagggaaagcggccatggtgggatacataagtgaaggggctgcccatTCAttattcctttgccctcggacg	PCR of KI cassette
gDNA SRCAP Fw	This paper	GTAGAGGAGTCAGAGGTAGAAG	Validation of KI on gDNA
gDNA SRCAP Rev	This paper	TGGTGGAAAGGAAGACAGC	Validation of KI on gDNA
Ypet Rev	This paper	GGAGACGTGGAGGAGAAC	Validation of KI on gDNA
P2A Fw	This paper	CGTTGTGGCTGTTGTAGTTG	Validation of KI on gDNA
SRCAP Fragment 1 Fw	This paper	CTACCCTCGTAAAACCGGTCGACatgcagagcagcccctccac	Cloning of wt and cd SRCAP
wtSRCAP Fragment 1 Rev	This paper	gccttcttgcttgggcactggctgcagcattctgttgaccttc	Cloning of wtSRCAP
cdSRCAP Fragment 1 Rev	This paper	ctgagcCGCAGCcagaataag	Cloning of cdSRCAP
wtSRCAP Fragment 2 Fw	This paper	gccagtgcccaagcaagaaggc	Cloning of wtSRCAP
wtSRCAP Fragment 2 Rev	This paper	gaagcagaatatgcgtttgtccgc	Cloning of wtSRCAP
cdSRCAP Fragment 2 Fw	This paper	ctgGCTGCGgctcagaacatcGCGaatttcaagtcccaacg	Cloning of cdSRCAP
cdSRCAP Fragment 2 Rev	This paper	ccactggagaacttggaggcag	Cloning of cdSRCAP
wtSRCAP Fragment 3 Fw	This paper	gcggacaaacgcatattctgcttcatcctttcaactcgaagtg	Cloning of wtSRCAP
cdSRCAP Fragment 3 Fw	This paper	gcctccaagttctccagtgggcccagctccaggtcacacactg	Cloning of cdSRCAP
SRCAP Fragment 3 Rev	This paper	CGCCCTTGCTCACCATGTCGACTCCcgtcttggcctttcgacctctgtg	Cloning of wt and cd SRCAP
TRE3G Fw	This paper	gtcttataccaactttccgt	Screening of SRCAP vectors
SRCAP Rev	This paper	cacattgctccagaactgcc	Screening of SRCAP vectors
SRCAP Fw	This paper	cctgacaccactcctagcctg	Screening of SRCAP vectors
mCherry Rev	This paper	gccgttcacggagccctcc	Screening of SRCAP vectors

Table S5. List of pioneer transcription factors

Name	Reference
AP-1	Lemma et al. Epigenetics and Chromatin 2022
ASCL1	Lemma et al. Epigenetics and Chromatin 2022
ATF4	Peng et al. eLife 2024
BACH1	Peng et al. eLife 2024
BCL6	Peng et al. eLife 2024
CEBPA	Peng et al. eLife 2024
CEBPB	Peng et al. eLife 2024
CEBPD	Peng et al. eLife 2024
CEBPG	Peng et al. eLife 2024
FLI1	Lemma et al. Epigenetics and Chromatin 2022
FOS	Peng et al. eLife 2024
FOSL2	Peng et al. eLife 2024
FOXA1	Peng et al. eLife 2024
FOXA2	Peng et al. eLife 2024
FOXA3	Peng et al. eLife 2024
FOXD3	Lemma et al. Epigenetics and Chromatin 2022
FOXE1	Lemma et al. Epigenetics and Chromatin 2022
FOXK2	Peng et al. eLife 2024
FOXM1	Lemma et al. Epigenetics and Chromatin 2022
FOXO1	Lemma et al. Epigenetics and Chromatin 2022
GATA1	Peng et al. eLife 2024
GATA2	Peng et al. eLife 2024
GATA3	Lemma et al. Epigenetics and Chromatin 2022
GATA4	Peng et al. eLife 2024
GATA5	Lemma et al. Epigenetics and Chromatin 2022
GATA6	Lemma et al. Epigenetics and Chromatin 2022
GRHL1	Lemma et al. Epigenetics and Chromatin 2022
GRHL2	Lemma et al. Epigenetics and Chromatin 2022
HLF	Peng et al. eLife 2024
HMBOX1	Peng et al. eLife 2024
HNF4A	Peng et al. eLife 2024
IKZF1	Peng et al. eLife 2024
JUNB	Peng et al. eLife 2024
JUND	Peng et al. eLife 2024
KLF4	Lemma et al. Epigenetics and Chromatin 2022
LEF1	Peng et al. eLife 2024
MAFF	Peng et al. eLife 2024
MAFG	Peng et al. eLife 2024
MEF2A	Peng et al. eLife 2024
MYB	Lemma et al. Epigenetics and Chromatin 2022

NFATC3	Peng et al. eLife 2024
NFE2	Peng et al. eLife 2024
NFE2L1	Peng et al. eLife 2024
NFIL3	Peng et al. eLife 2024
NR2F1	Peng et al. eLife 2024
NR5A1	Peng et al. eLife 2024
NF-Ya	Lemma et al. Epigenetics and Chromatin 2022
OTX2	Lemma et al. Epigenetics and Chromatin 2022
PAX7	Lemma et al. Epigenetics and Chromatin 2022
PBX1	Lemma et al. Epigenetics and Chromatin 2022
PBX2	Peng et al. eLife 2024
POU5F1	Lemma et al. Epigenetics and Chromatin 2022
PPARG	Peng et al. eLife 2024
RUNX1	Lemma et al. Epigenetics and Chromatin 2022
RUNX3	Lemma et al. Epigenetics and Chromatin 2022
RXRB	Peng et al. eLife 2024
SOX2	Lemma et al. Epigenetics and Chromatin 2022
SOX9	Lemma et al. Epigenetics and Chromatin 2022
SPI1	Lemma et al. Epigenetics and Chromatin 2022
SRF	Peng et al. eLife 2024
STAT3	Peng et al. eLife 2024
TEAD1	Peng et al. eLife 2024
TFAP2C	Lemma et al. Epigenetics and Chromatin 2022
TP53	Lemma et al. Epigenetics and Chromatin 2022
TP63	Lemma et al. Epigenetics and Chromatin 2022
ZNF24	Peng et al. eLife 2024